EXPERIMENTATION AND MODEL DEVELOPMENT OF HIGH TEMPERATURE SHAPE MEMORY ALLOY ACTUATION CYCLING UNDER TENSION, COMPRESSION, AND BENDING

A Thesis

by

DANIEL THOMAS MARTIN

Submitted to the Office of Graduate and Professional Studies of
Texas A&M University
in partial fulfillment of the requirements for the degree of

MASTER OF SCIENCE

Chair of Committee,	Dimitris C Lagoudas
Committee Members,	Darren Hartl
	Ibrahim Karaman
Head of Department,	Rodney Bowersox

December 2019

Major Subject: Aerospace Engineering

ABSTRACT

Shape Memory Alloys (SMAs) are a unique class of intermetallic alloys that can cyclically sustain large deformations and recover a designed geometry through a solid-to-solid, martensitic phase transformation. The multifunctional behavior of SMAs, being both structural and active, along with a favorable actuation energy density, make SMA actuators practical for volume, mass, and mechanical improvements to a system. For aerospace engineering applications, High Temperature SMAs (HTSMAs) are specialized to operate in the extreme environmental conditions necessary for safe operation in a higher temperature range. The main limitations to HTSMAs, however, are the unpredictable cyclic response and stability, large scale manufacturing inconsistency, and lack of commercially available design tools to accurately capture the macroscopic response. This study will address these limitations by characterizing cyclic evolution, using a single extrusion of high temperature SMA material for manufacturing and property consistency, and by developing and validating a finite element model to predict cyclic actuation response in bending loading conditions typical in SMA actuator components. Results show experiments for $Ni_{50.3}TiHf_{20}$ High Temperature SMA (HTSMA) including: differential scanning calorimetry, thermomechanical actuation cycling in tension and compression, thermomechanical actuation cycling under pure bending, and C-Ring bending. Since there is significant tension - compression asymmetry in SMA phase transformation, a full-field strain response is quantified for bending cases using Digital Image Correlation (DIC). The four point bending results contain a neutral axis shift due to the asymmetry, and during actuation cycling, the

neutral axis continues to shift as a consequence of remnant, unrecovered plastic strains. C-ring tests show the martensitic phase transformation initiate in tension followed by compression during forward phase transformation. Lastly, two phenomenological, macroscopic SMA constitutive models that address cyclic behavior and anisotropy in SMA actuation are addressed. The constitutive models are used in a finite element software, Abaqus, with a user-defined material subroutine (UMAT) to address model improvements in light of the experimental results. Needed updates to the UMAT are discussed that will improve accuracy and prediction of the SMA actuation response in bending.

CONTRIBUTORS AND FUNDING SOURCES

Contributors

This work is supervised by a thesis committee consisting of Professor Dimitris Lagoudas, Professor Darren Hartl, and special appointee James Mabe of the Department of Aerospace Engineering, as well as Professor Ibrahim Karaman of the Department of Material Science.

The user-defined material subroutines used in Section 4 are provided by Professor Dimitris Lagoudas and Professor Darren Hartl published in 2019 and 2018, respectively.

All other work for the thesis is completed by the student independently.

Funding Sources

This work is supported by the National Aeronautics and Space Administration (NASA) through the University Leadership Initiative (ULI) project under the grant number: NNX17AJ96A. The conclusions in this work are solely made by the author and do not necessarily represent the perspectives of NASA.

TABLE OF CONTENTS

Page

LIST OF FIGURES

Page

LIST OF TABLES

Page

1. INTRODUCTION AND LITERATURE REVIEW

1.1 Shape Memory Alloys

Shape Memory Alloys (SMAs) exhibit a reversible solid-to-solid phase transformation between the austenite and martensite phases, accessed through inputs of stress, temperature, or a thermomechanical combination. Although SMAs have a lower actuation frequency compared to other active materials, they are useful in actuation applications due to their large energy density, and their ability to recover extremely large transformation strains. In other words, SMA actuators can undergo recoverable shape changes under high stress levels and produce a large work output compared to other solid state actuator materials, such as piezoelectric ceramics or shape memory polymers, shown in Figure 1 [3].

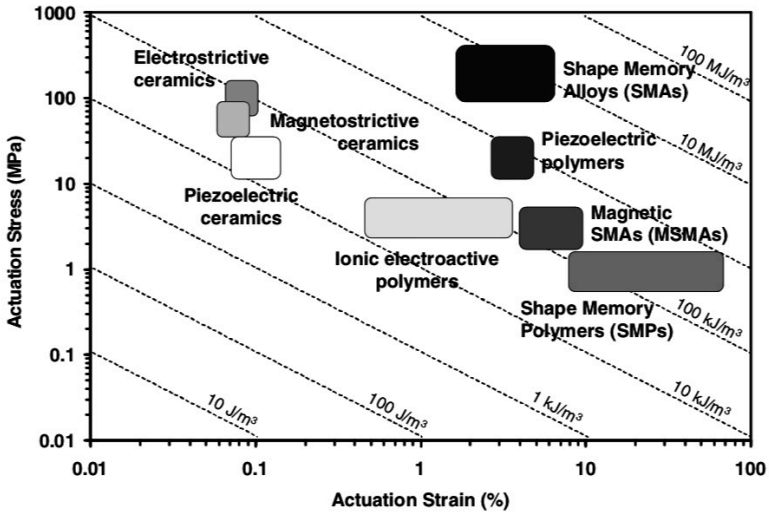

Figure 1 Actuation Energy Density comparing common active materials reprinted from [3].

Shape Memory Alloys can be characterized based on their phase transformation between the austenite and martensite phases by a phase diagram, shown in Figure 2. The four critical transformation temperatures, M_f, M_s, A_s, A_f, describe the beginning and final transition of the SMA between the two phases. Depending on the material composition, heat treatment, and processing, the transformation temperatures can be modified to be below freezing, or even well above 85°C. The martensite phase is further broken down into twinned martensite and detwinned martensite. For twinned martensite, the mechanical load applied to the SMA is not high enough to see a macroscopic deformation, only a lattice structure rearrangement. On the other hand, the detwinned martensite phase shows a significant deformation compared to the austenite phase, between 1% to 10% macroscopic strains. The stress that initiates detwinned martensite is specified at, σ^s, and the full martensite transformation at σ^f [3].

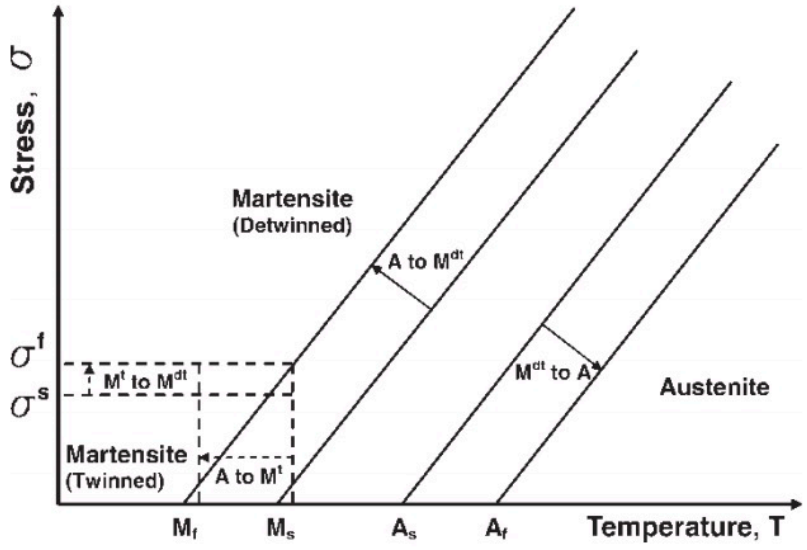

Figure 2 Theoretical SMA stress - temperature phase diagram reprinted from [4].

The thermomechanically induced phase transformation of an SMA under a constant load is shown in Figure 3. It is a recoverable deformation controlled by simple temperature inputs, and it allows for the SMA to actuate between the detwinned martensite phase and the austenite phase. This study will address the macroscopic response of SMAs using this thermomechanical actuation in tension, compression, and bending.

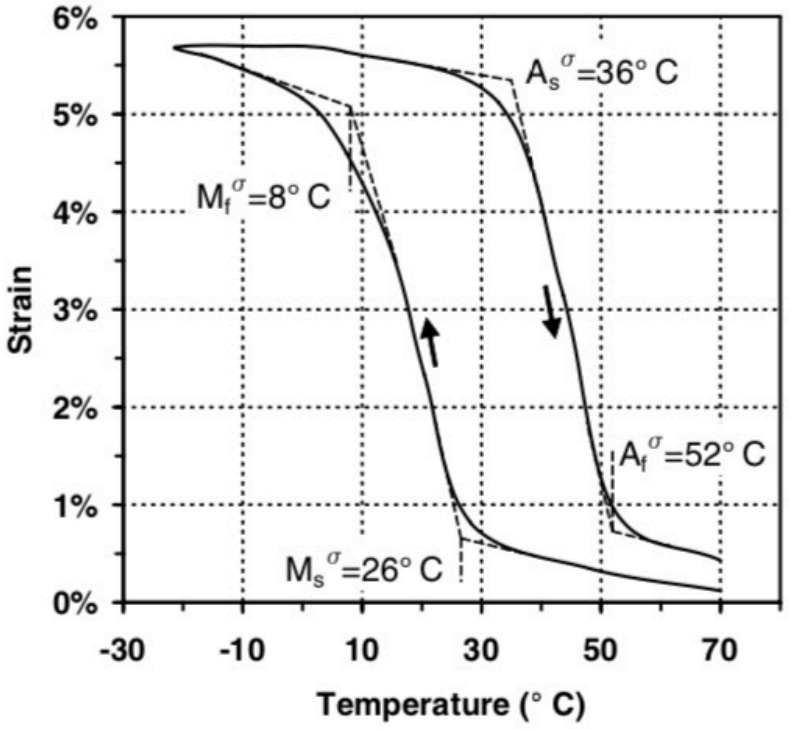

Figure 3 Constant load phenomenological transformation reprinted from [3].

1.1.1 Aerospace Applications of Shape Memory Alloy Actuators

SMAs are implemented in numerous commercial and industrial fields including: automotive, aerospace, electrical, robotics, and biomedical, and they can take the form of motors, actuators, transducers, structural materials, or sensors [5].

The biomedical field holds the largest amount of patents and functional uses of SMAs thus far, but as the depth of understanding and manufacturing costs decrease, aerospace applications are growing, even within the restrictions of the Federal Aviation Administration. Since aircraft and spacecraft require many complex systems, the multifunctionality of SMA components have the potential to reduce complexity, volume, weight, and sometimes cost, compared to traditional electromechanical or hydraulic actuator systems [4]. Some specific examples of SMA actuator applications for the aerospace industry are morphing wings, variable geometry chevrons, deployable solar panels, or active space radiators [6-12].

Sofla *et al.* have completed a comprehensive review of wing morphing technologies using antagonistic SMA-actuated flexural structural forms to actively bend and twist a wing for improved aerodynamic performance [6]. The SMA actuators are capable of enduring the aerodynamic loads, satisfy power requirements, and achieve the force and torque required for a small unmanned aircraft [7]. They show that SMAs can be incorporated in advanced systems without weight penalties or stiffness loss compared to conventional actuators.

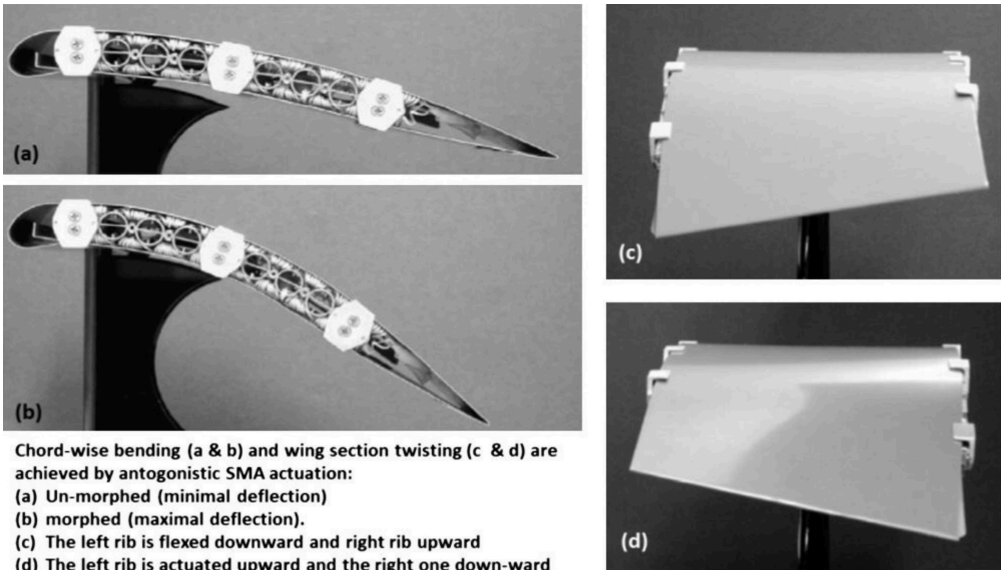

Figure 4 Wing morphing with antagonistic SMA actuators reprinted from [6].

The Boeing variable geometry chevron utilizes bending actuation of SMAs in order to utilize a trade-off between noise mitigation at take-off and landing and engine performance at high altitude for a 787 engine. Instead of a static chevron, the alternative design uses passively controlled SMA actuators to adjust engine properties with changes in altitude. At low altitudes, the chevron is in a noise reduction configuration, and at high altitudes, the chevron relaxes to recover engine performance [8-10].

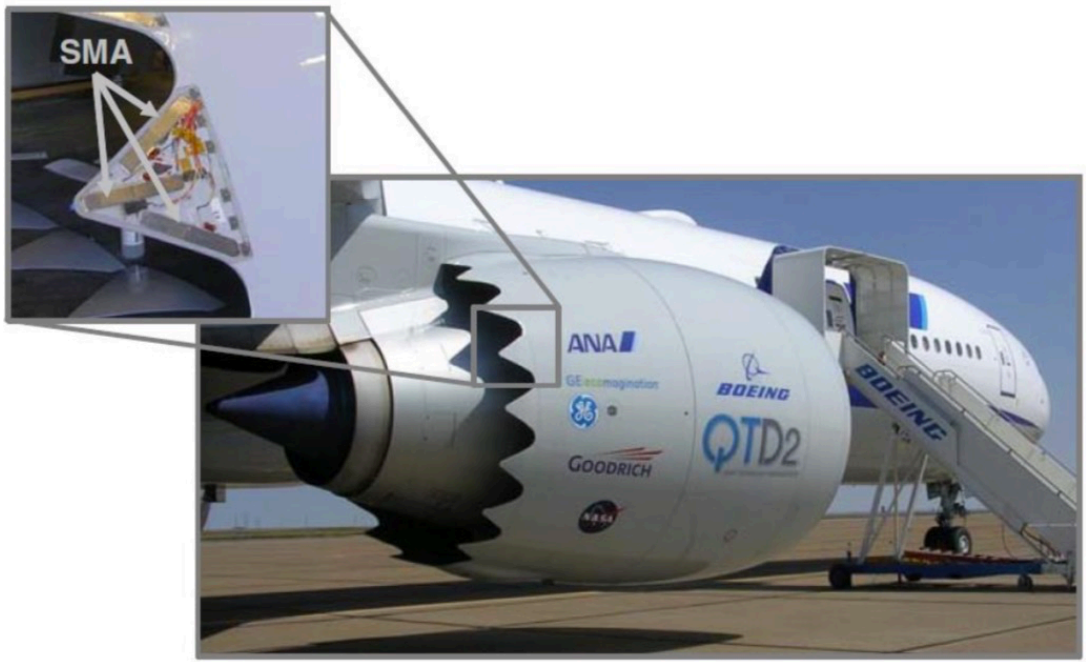

Figure 5 SMA Actuated Chevron on Boeing aircraft reprinted from [10].

The reconfigurable solar array uses an SMA torque tube to deploy and retract a microsat solar array system. The project showcases an SMA's ability to reduce the weight, volume, and complexity of the system using SMAs instead of the conventional system using electronic actuators. It also satisfies control requirements where it could be deployed at low temperatures under 60 seconds with a total twist angle of 46 degrees. A prototype was built to prove the technology and the theory [11].

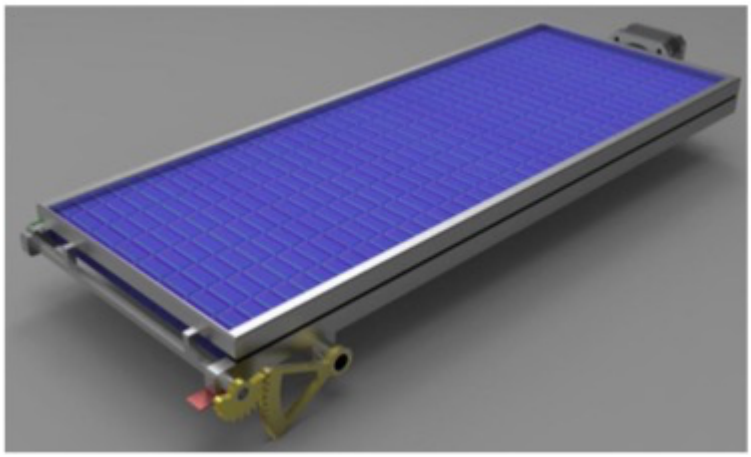

Figure 6 Solar array design in a stored state reprinted from [11].

SMAs are practical for space applications as well. Space radiators are important for thermal control in crewed spacecraft design, but they require high turn down ratios needed for a large range on heat rejection rates. A novel radiator concept has been designed, analyzed, and fabricated using SMA material for passive geometric reconfiguration by Bertagne *et al*. The radiator design allows for a 12:1 turndown ratio, compared to a 3:1 ratio used by current space radiators. SMAs could be used as sheets, strips, or wire forms to close and open the panel. At high temperatures, the radiation panel morphs into the maximum heat rejection shape, when temperatures decrease, the panel returns to a closed configuration, and the actuation process is fully-reversible [12].

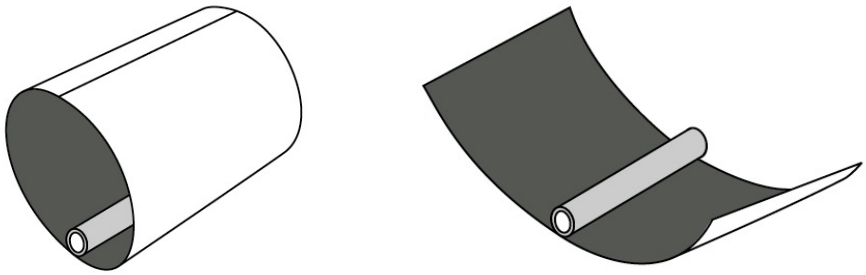

(a) (b)

Figure 7 Schematic representation showing morphing radiator panel in a closed shape (a) for minimum heat rejection and open shape (b) for maximum heat rejection reprinted from [12].

1.1.2 High Temperature Shape Memory Alloys

While NiTi is the most studied SMA due to its large recoverable strain and corrosion resistance, High Temperature SMAs (HTSMAs), such as the tertiary metal alloys NiTiHf and NiTiZr, are becoming the present research focus due to their application in higher temperature ranges, mostly for aerospace applications. These alloys have transformation temperatures well above 85°C, where current Radio Technical Commission for Aeronautics (RTCA) guidelines require components to be dormant in operation environments [13]. HTSMAs are also required to exhibit acceptable actuation strain recovery, long term stability, resistance to plastic deformation and functional fatigue, and corrosion resistance [14].

The NiTiHf alloy systems with more than 50 (at. %) nickel content shows enhanced mechanical and thermal stability as a result of the formation of precipitates compared to nickel lean NiTiHf. Depending on material purity, however, these alloys can suffer from large thermal hysteresis, low strength, unstable shape memory behavior,

and development of large residual strains from thermal cycling [15]. This material does not show other transformations in the martensite transition such as rhombohedral (R-phase) seen in nickel rich SMAs [16], bainite [17], or the rubber-like behavior [18].

1.1.3 Transformation Induced Plasticity

After cycling from the austenite phase to the detwinned martensite phases under a thermomechanical loading path, unrecovered strains develop after each cycle. Unlike plastic strains in conventional metals, these remnant strains occur at significantly lower stress levels, well below the yield limit, and lead to functional fatigue of the SMA actuator. These remnant strains are due to the combination of transformation induced plasticity (TRIP) and retained martensite. TRIP is defined as the plastic flow arising from solid state phase transformations involving shape changes at low stress levels. It is an evolutionary phenomenon during thermomechanical cycling of SMAs that leaves a number of permanent microstructural changes during the forward transformation into martensite [3]. It is extremely prominent in the early stages of the fatigue life of the SMA or HTSMA actuator, but the development of unrecovered strain slows once dislocations reach the grain boundaries and the martensite variants stabilize. Also, TRIP is dependent on material processing and testing procedures, such as heat treatment or upper cycle temperature. It has been seen in experiments and implemented in 3-D macroscopic constitutive models, but the characterization process must include the determination of cyclic evolution parameters in order to capture this phenomenon accurately; these will be discussed further in Section 4.2.

1.1.4 Two Way Shape Memory Effect

Additionally, the material system tested in this study is shown to exhibit the two-way shape memory effect (TWSME). The TWSME is a phenomenon that exhibits a reversible, external shape change without mechanical loading, generated by thermally cycling or training the SMA actuator [20]. TWSME is not fundamental to SMAs, but under the right microstructural conditioning, SMAs generate internal stresses that will allow for the actuation process between austenite and specific martensite variants to take place [21]. This phenomenon can be difficult to produce and is not seen in all applications of thermomechanically induced actuation cycling. For example, at high cycling temperatures, microstructural features that allow for TWSME can be erased. Or, if the material is brittle, then the dislocations will not move as easily, preventing the formation of internal stresses at early cycling stages. Since this process is seen macroscopically and is implemented in the current phenomenological model that is discussed, the back stress parameters that govern the TWSME need to be calibrated to ensure the generation of internal stresses is incorporated [22].

1.1.5 Tension – Compression Asymmetry

Previous experiments have shown that polycrystal and single crystal SMAs have a significantly different macroscopic response in compression compared to tension. Researchers studying polycrystalline NiTi show compressive loading states result in smaller displacements, higher transformation stress levels, and strain hardening, formed at the single crystal level [23-24]. The phenomenon is mostly attributed to the effect of the resolved shear stress state on martensite twinning and macroscopic modes of

deformation. Since the transformation initiates from a critical resolved shear stress, in the same direction of the prescribed transformation direction, there is a unidirectional dependence to the phase transformation. This creates a considerable orientation dependence and a different critical transformation stress depending on loading direction for polycrystal SMAs with a strong crystallographic texture [25]. For macroscopic modes of transformation, tension stress states lead to a nonuniform, localized martensite reorientation that propagates at a constant applied load; in compression, however, there is no localized transformation and propagation of martensite is reduced [26].

In order to accurately characterize the bending response described later, tension-compression asymmetry is experimentally studied to determine the impact on prediction and evolution in multiaxial loading conditions. Since polycrystal HTSMA is being tested and the texture is not quantified, relationships to micromechanical models or single crystal tension - compression phenomenon cannot be determined.

1.2 Objectives and Impact

The NASA University Leadership Initiative (ULI) has awarded a grant to study applications that can potentially reduce ground level influence from the sonic boom, generated from supersonic civil aircraft, in order to meet a ground level noise limitation of 75 PLdB. It has been shown that small changes in the outer mold line of supersonic aircraft can have significant impacts on the sonic boom [27]. Boom minimization theory proves that in flight outer mold line changes have the potential to minimize the shock pressure rise or the over-pressure of the ground signature [28, 29]. Since perceived loudness is sensitive to atmospheric fluctuations and the shock pressure rise or

overpressure, the introduction of controllable morphing structures on the aircraft can provide the in-flight outer mold line changes needed to minimize ground level influences [30]. HTSMA studies involving material processing, function fatigue, and constitutive model development are currently being funded as part of the NASA ULI as a potential morphing actuation solution.

Figure 8 NASA X-series supersonic civil aircraft concept.

The motivation of this study is to satisfy requirements for design and optimization of HTSMA actuators for the NASA ULI program, but also to make SMAs commercially viable, and reduction in development cost is a high priority. For example, a costly method would be designing, building, testing, iterating, and then optimizing prototypes; whereas, the preferred and more efficient method to design SMA actuators

would be characterization, analysis, and optimization before physical construction and prototyping begins. This method saves material and time in the design phase and is a necessity for scaling up production. This study will focus on experiments to develop cost effective SMA constitutive models and design tools for early stages in the NASA ULI program.

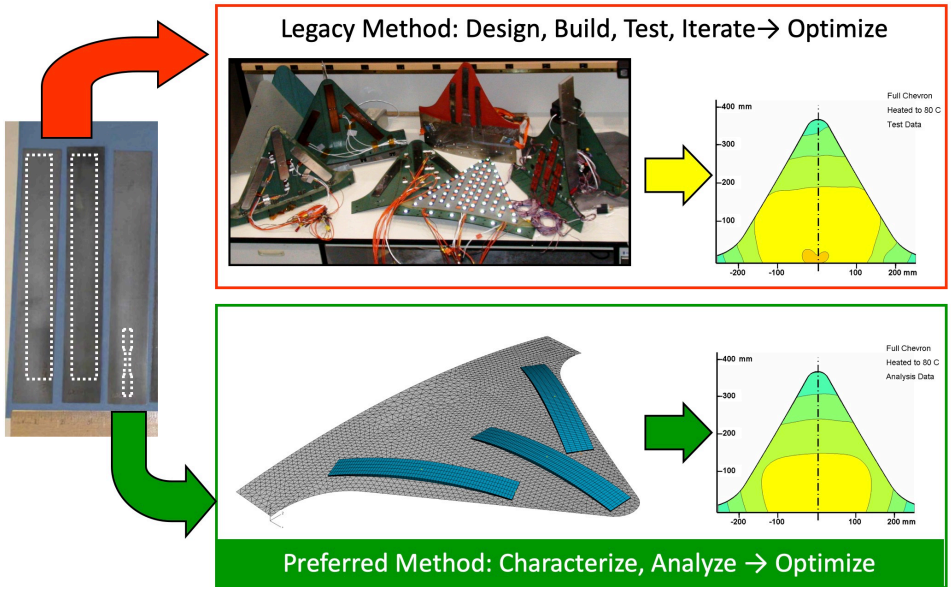

Figure 9 SMA actuator design methods reprinted from [10].

This study highlights constant load, SMA actuation experiments for the development and validation of phenomenological, macroscopic constitutive models for polycrystal HTSMAs. The development of a proven prediction method for the evolution of SMAs is crucial for structural design applications, actuator training and implementation, optimization routines, and actuator control. These improvements to

SMA modeling efforts provide necessary steps towards SMA technology and morphing actuators.

Novelty of this work includes experimental tension-compression asymmetry in thermomechanical actuation, cyclic actuation under pure bending, and C-Ring actuation experiments for HTSMAs. The phenomenological constitutive models used have new capabilities that are addressed in detail, and simulations of the experiment are replicated as close as possible to highlight the capabilities of the design tools.

2. EXPERIMENTAL DESIGN

2.1 Overview

This section specifies the testing methodology, diagnostics, and equipment used to test HTSMAs under thermomechanical actuation. The main objectives are to use measurement techniques consistently, use the same material and material processing methods, and provide experimental repeatability. Detailed below is the material selection, specimen geometry and design, heat treatment procedure, and experimental setups for thermomechanical actuation testing of $Ni_{50.3}TiHf_{20}$ (at. %) HTSMAs.

Each experiment is determined based on the needed parameters from the characterization procedure described in Section 4.2, as well as previous SMA testing methods and ASTM standardization [31]. Some existing ASTM standards for testing SMAs include: ASTM F2004 for differential scanning calorimetry, ASTM F2082 for bend and free recovery tests, and ASTM F2516 for tensile testing of SMAs with a focus on super-elasticity [32-34]. Although these tests are general and mainly apply for medical industry SMA applications, they are being utilized as a guide for experimentation and fixture design. For example, ASTM E08 is being used for the specific material parameters and specimen design for uniaxial tensile testing, but the specific implementation of detailed procedures has not been published for the thermomechanical actuation experiments in this study [31, 35].

Some of the experiments in this study are conducted in a similar method done by previous researchers, and on similar test setups. The uniaxial tensile testing using

thermal cycling with a constant dead load has been utilized recently to study functional fatigue [16, 36], damage propagation [37], influences of upper cycle temperature [38], and TWSME [39]. The procedures and control systems used are nearly identical and have been developed and calibrated over the last five years to provide consistent actuation experimentation of high temperature SMAs. Although there is not a standard test procedure to follow, the previous studies provide a respectable reference for specimen design, material preparation, and actuation test procedures.

2.2 Specimen Geometries, Processing, and Preparation

2.2.1 Material

The $Ni_{50.3}Ti_{29.7}Hf_{20}$ (at. %) material is received from the Boeing company as part of the NASA ULI program. Before processing, the high temperature SMA material is a single, 10.16mm diameter, extruded rod. This material system has been tested before, but has shown significant batch to batch variation in material properties, structural response, transformation temperatures, and compositional impurity. The focus of this study is not on the differences between the material systems, but the unpredictable variation in material response means the characterization process is necessary for each batch of NiTiHf. All of the specimens tested are taken from the extruded rod to minimize manufacturing discrepancies and batch to batch variation.

2.2.2 Dogbones Specimens, Compression Specimens, Plate Specimens, C-rings

From the extruded rod, the specimens are all cut using wire electro-discharge machining (EDM) [40]. This process leaves a recast layer on the surface of the specimens that causes small, but non-critical surface defects. Since all of the specimens

are machined using the same method and in the same direction, the variation between specimens is reduced.

Each specimen was designed specifically for each experimental setups, and they depend on testing standards, heating application, and loading path. The flat dogbones are used in uniaxial tension tests for characterization. The large surface area sections allow for mechanical grips and electrical leads to be attached without influencing the gauge section. The cross sectional area is small enough for resistive heating to efficiently heat, and convective cooling to quickly cool the gage section, but large enough to warrant a bulk material response.

The compression specimens are designed as cylinders with a diameter to height ratio of 0.5. These specimens are used in an MTS Insight machine with a thermal oven to apply constant load loading and a gradual temperature change, described in Section 2.3.5. The compression specimens have a diameter of 3.81mm and a height of 7.62mm.

The plates are designed to fit the custom built, four point bending fixture detailed in Section 2.3.6. The holes at the end allowed for the electrical cables to be connected, but the length of the specimens minimized the influence from the leads. These plates have a cross section of 9.525mm by 2.108mm.

Lastly, C-ring specimens are made from the extruded rod with holes drilled from the top through the bottom in order to mount the specimen for compressive testing. The specimen has two planes of symmetry with a thickness of 1.5mm and a depth of 19mm.

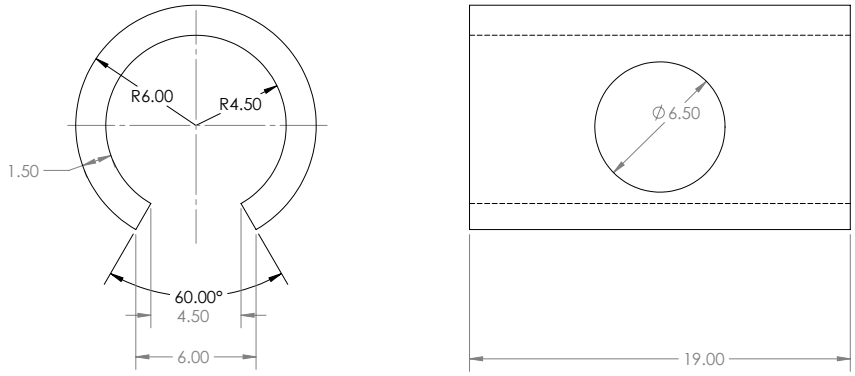

Figure 10 Dimensions, in millimeters, of the C-ring specimen.

2.2.3 Heat Treatment Procedure

The $Ni_{50.3}Ti_{29.7}Hf_{20}$ is heat treated to match the previous preparation and heat treatments studies on a similar material system. It is cleaned with acetone, wrapped in tantalum foil, and vacuum sealed to 3.0E-5 torr in a quartz tube. It is not homogenized due to the extrusion process providing a high temperature homogenization, but a heat treatment of 550℃ for 3 hours followed by water quenched is performed. Previous studies on this material under tensile stresses showed that this heat treatment results in superior stability of actuation strain and very small TRIP strains [41-44]. This study does not consider the influence of heat treatments and only warrants consistent material preparation.

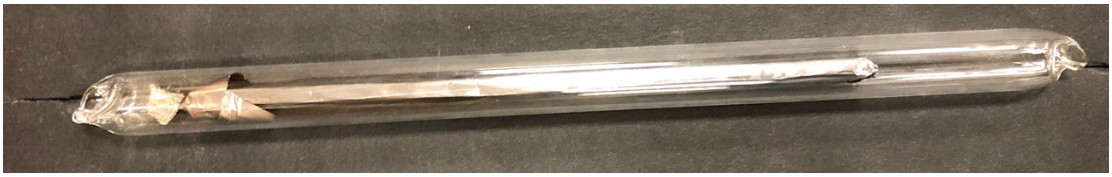

Figure 11 Vacuum sealed plate wrapped in tantalum foil in a quartz tube.

2.3 Experimental Setups

2.3.1 Testing Methodology

Displacement measurements are held constant through each experiment by using Digital Image Correlation (DIC) with similar post-processing methods to gather full field or single direction displacement data, checked against a linear variable differential transformer (LVDT). Furthermore, the temperature is measured using a K-type thermocouple, calibrated by matching the signal to three reference temperatures in a stabilized furnace. The same thermocouple is used for each experiment for surface temperature measurements in the transformation region.

Three different testing setups are utilized in order to capture the response of the NiTiHf material system. Each setup has different testing challenges and material specimens. A crosshead controlled, MTS material testing system and two custom built load frames are used with compression, dogbone, and plate specimens.

Unfortunately, there are some limitations to testing capabilities that forced certain test procedures. First, temperature application is different for the custom built load frames that use Joule heating and convective cooling, compared to the compression and C-ring experiments that used a thermal oven or induction heating. The difference

results in a significantly different heating and cooling rate for the tension - compression asymmetry experiment. Second, SMAs can be difficult to grip using standard testing fixtures. The uniaxial tension tests are tested on a custom built frame where the temperature at the grips could be controlled with Joule heating to avoid phase transformation in that region. Lastly, the uniaxial tension, four point bending, and C-ring tests are performed on custom made test frames, liable and sensitive to human interactions. There are many tests performed that resulted in specimen overheating, twisting, or out of plane loading that are not shown. The results shown below only consider the tests where these human inflicted errors are minimized and consistent results are achieved.

2.3.2 Temperature Measurements

The main measurements needed are temperature and displacement of the SMA. In order to capture temperature accurately, the same contact thermocouples and data acquisition system is used for each experiment. For temperature measurements, traditional contact thermocouples, along with non-contact infrared sensors are used for redundancy. Due to the importance of precision and accuracy for these tests, these measurement techniques are compared to show that these measurement techniques are valid for experimenting HTSMAs.

The K-type contact thermocouples matched the IR sensor calibration after setting up the cold junction compensation (CJC) temperature measurement using a custom scaled voltage reading and thermocouple settings in Labview [45].

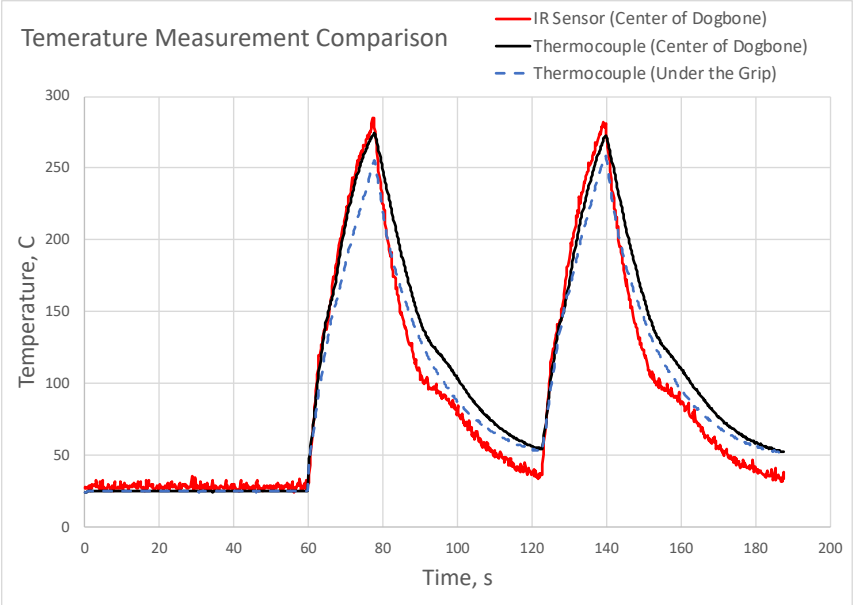

Figure 12 Surface temperature measurement comparison on a flat dogbone using the IR sensor and two thermocouples to quantify error and temperature gradients.

2.3.3 Digital Image Correlation and Linear Variable Differential Transformer

The diagnostic methods used for displacement measurements are digital image correlation (DIC) and a linear variable differential transformer (LVDT). Digital Image Correlation, or DIC, is used in each experiment to optically measure displacement. The cameras, software, and analysis methods came from Correlated Solution, a non-contact measurement company. The specimens require a random speckle pattern to be affixed on the surface of the material for the software to analyze the change in the pattern from the reference image. A high temperature spray paint is used to cover, and then speckle the surface of the specimen. An example of the speckle pattern is shown in Figure 13 and 14 below. During testing, a reference image is taken before any loads are applied to the material, and then a series of pictures are taken at a 0.5 second to 5 second intervals

throughout the experiments. The output generated after each picture provides full field displacement measurement, as well as total extension and engineering strain. If certain regions are more interesting to evaluate, displacement and strain values could be extracted at single points or small regions. For example, the lines labeled E0, E1, and E2 placed on the specimen in Figure 13 can be utilized to calculate the uniaxial extension of the specimen based on the reference image, acting as a non-contact extensometer. DIC equipment and processing is used consistently throughout the experiments presented with a subset size of 21 pixels and step size of 7.

Figure 13 Digital image Correlation speckle pattern used on a flat dogbone for uniaxial tension testing and non-contact extensometer analysis.

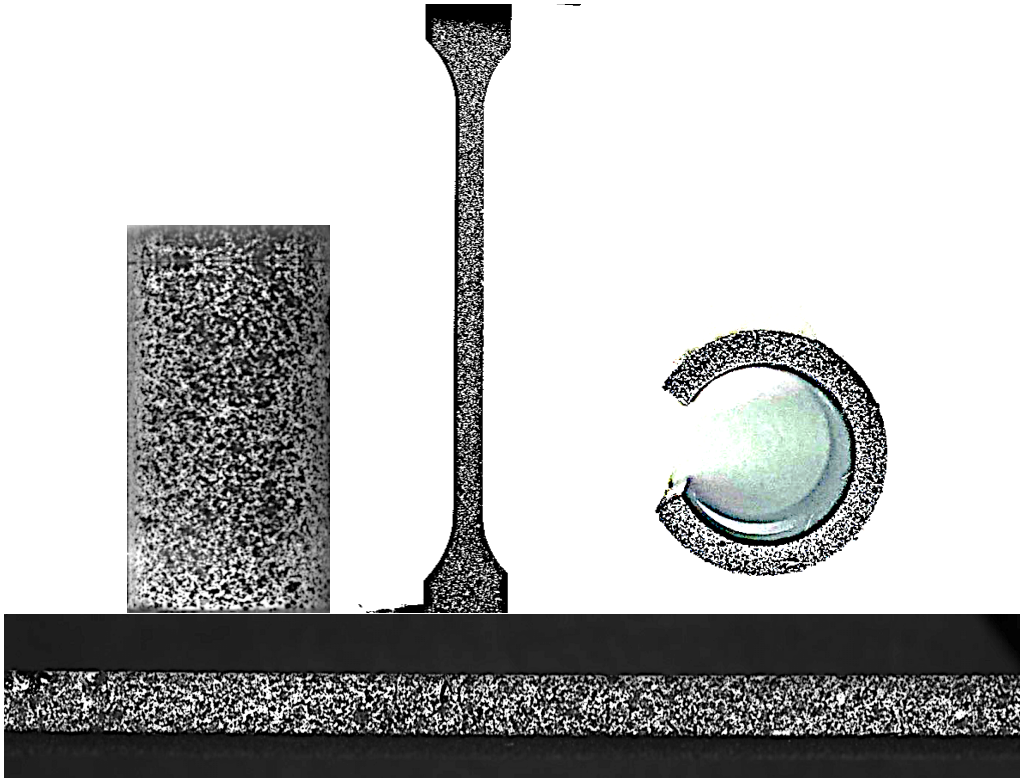

Figure 14 High fidelity speckle patterns on different specimens (These images are not to scale).

Comparing the DIC to the LVDT measurement shows that the two displacement measurements are reading similar values for each case on the custom built load frames. The small error shown is a result of the small grip region of the dogbone providing additional displacement.

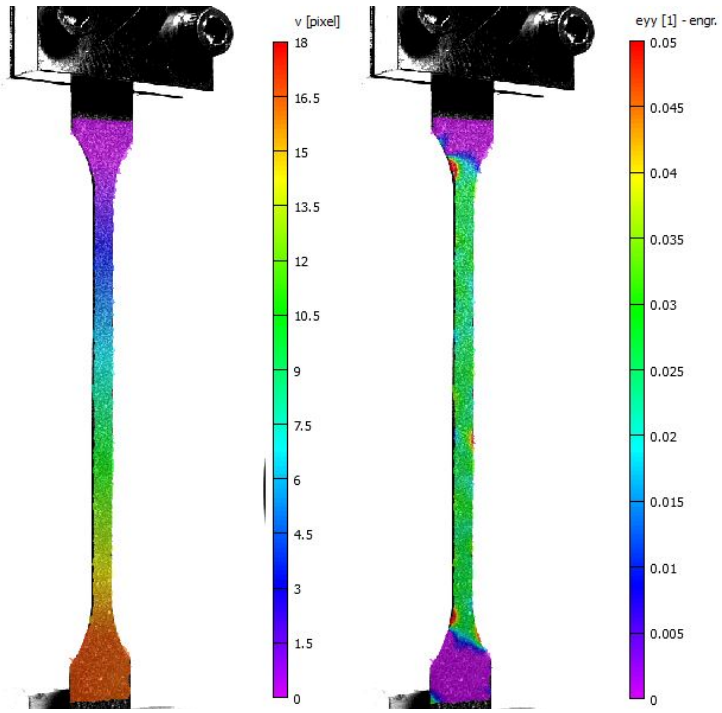

Average Strain: .03

(a) (b)

Figure 15 First actuation cycle vertical displacement (a) and vertical strain (b) calculation at the gauge section.

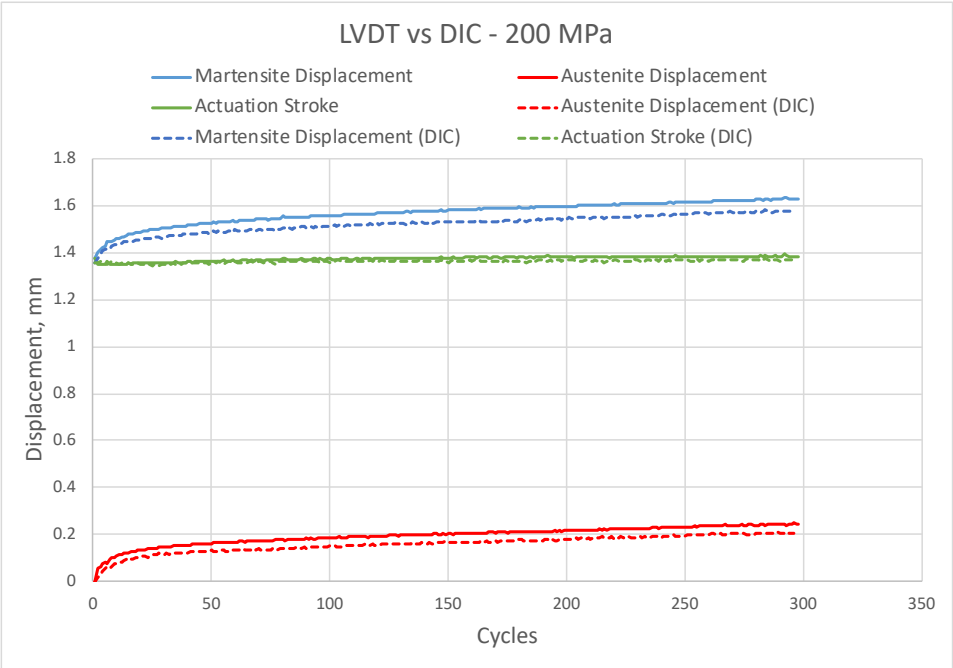

Figure 16 LVDT, total extension, and DIC comparisons in mm.

2.3.4 Uniaxial Actuation Tensile Testing

The uniaxial actuation testing is conducted on a custom built load control frame that allowed for continued cycling of flat SMA dogbones. The load frame, shown in Figure 17, can provide a constant load condition using a hanging dead load and controlled temperature cycling using resistive heating with an alternating current. The sensor data acquisition and temperature control are operated by an in-house LabView program. The diagnostics seen in the image below include an IR sensor and a contact thermocouple for temperature measurements, as well as the LVDT and DIC, not shown in the image, for displacement measurements. The load is connected directly to the bottom of the specimen grips to prevent any torsion. Computer fans are attached to the frame to provide continuous forced convection; in the work by Wheeler [16], forced convection during heating also reduces temperature gradients.

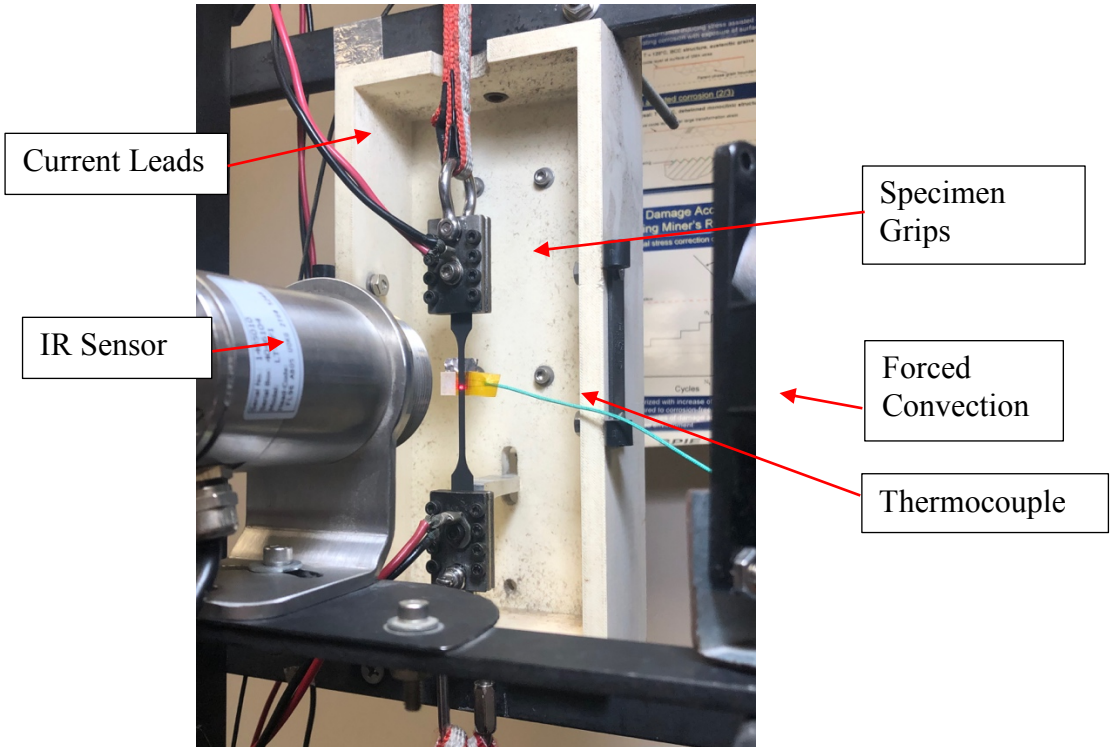

Figure 17 Actuation fatigue tensile testing setup.

The power system consists of a variable alternating current power supply (VARIAC) with a 130V manually tunable range, a transformer, a control box with a solid-state relay, and two pairs of electrical leads attached to the specimen grips. The grips can be tightened manually, but it is important to use a guide to prevent any twisting or bending in the dogbone when attaching the electrical leads or applying the dead load, shown in Figure 18. This system supplies between 10 and 40A to the actuator at 0.5 to 4V.

Figure 18 Grip system and guide.

2.3.5 Compression Testing

Compression tests are conducted on a MTS Insight machine using a compression plate fixture. There are two modes of control available on the insight machine: load control and displacement control. Displacement control is the desired method with the MTS Insight machine and the most accurate. For this control, a crosshead displacement rate of 0.1 mm/min is used for quasi-static testing. For actuation tests, displacement control is used to reach the desired fixed load, and then load control is used to maintain the load with a PID controller, as shown in Figure 19. The PID parameters used for load control are shown in Figure 20. These are tweaked manually until the load cell produced a maximum error of 15.8N. The cycling control is much slower to avoid temperature gradients in the specimen, test fixture, and thermal chamber. Temperatures are extracted using three thermocouples to determine the magnitude of the temperature gradients.

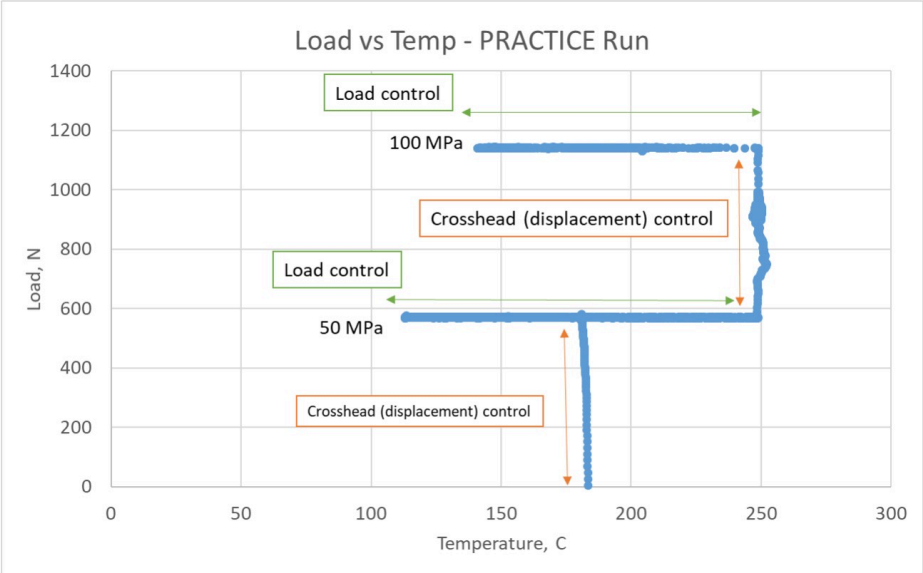

Figure 19 Load control and Displacement control procedure for MTS Insight machine for SMA actuation testing.

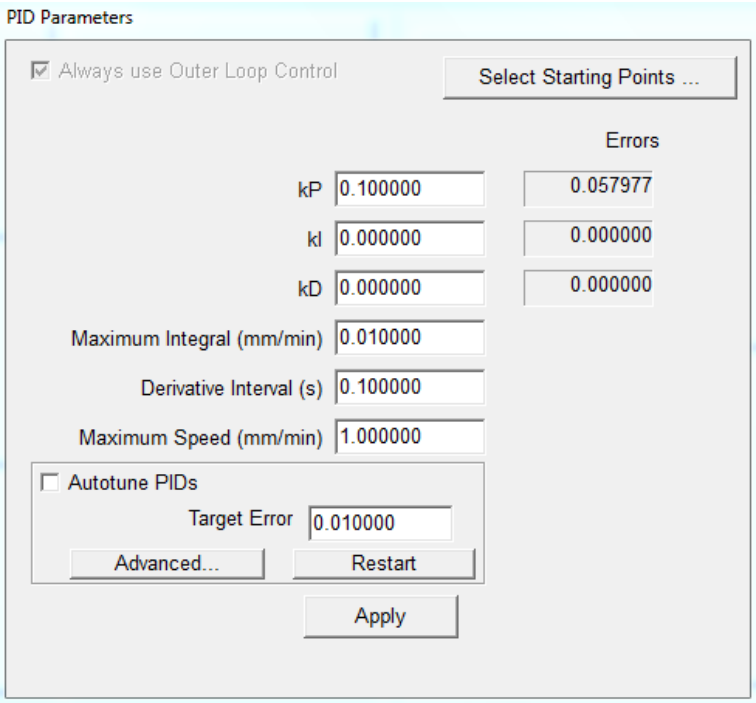

Figure 20 PID parameters used for load control.

2.3.6 Four-Point Bending Testing

The next test setup is specialized for four point bending tests. This frame is custom built and modified to provide cyclic actuation testing under dead loads. In order to customize for the large transformation deflection and for a cheap alternative to traditional bending fixtures, the test fixture is made using VeroWhite 3D printed material with stainless steel contact points and painted to allow for background contrast for DIC imaging. The stainless steel contact points do not rotate during the test in order to provide symmetry and minimized out of plane motion. The diameter of the supports and load points allow for the specimen to bend uniformly and consistently between actuation cycles. The fixture, as well as the load point, is leveled and balanced. This frame could also be used for 3 point bending, but this research focuses on four point bending in order to have a pure bending loading path and to simplify the model validation procedure.

In order to have similar testing procedures, the 4 point bending test uses the same power supply as the uniaxial actuation tension tests. The power system consists of a variable alternating current power supply (VARIAC) with a 130V manually tunable range, a transformer, a control box with a solid-state relay, and two pairs of electrical leads attached directly to the specimen. After applying the alignment load, 1.85N, to the beam, actuation tests show that the leads are not influencing or loading the specimen as long as they have free range of motion throughout the experiment.

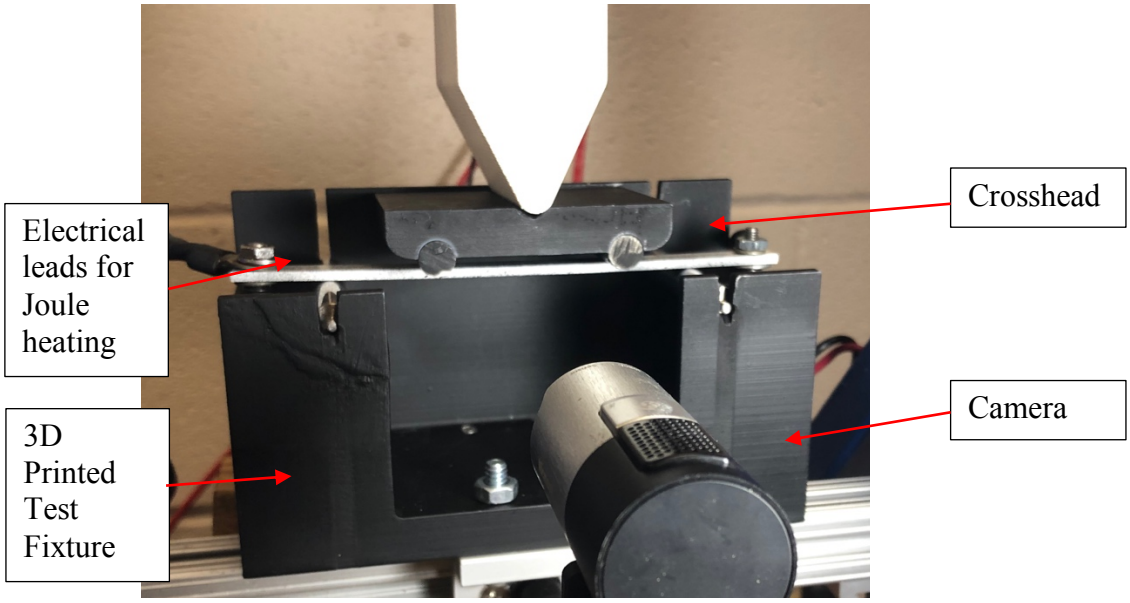

Figure 21 Four point bending fixture.

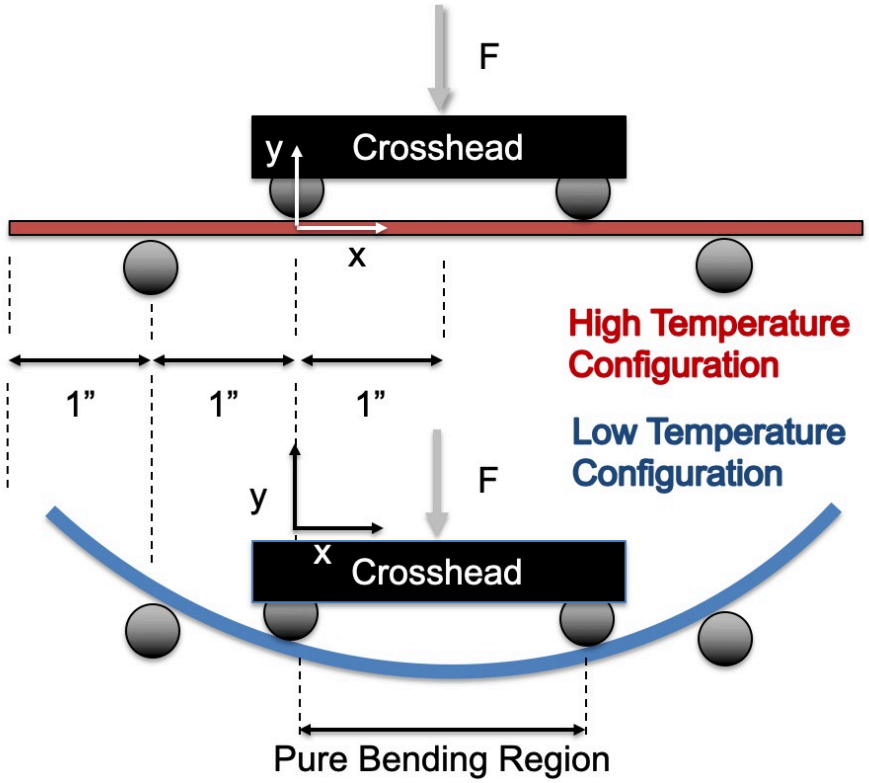

Figure 22 Graphic of the four point bending test.

2.3.7 C-ring Test Setup

The C-ring geometry is mainly used for corrosion - fatigue experiments because it contains a compression and tension face. Some applications of the geometry utilized the C-ring as a pressure seal, similar to the O-ring. The C-shaped cross section allows significant deformation to take place under low to moderate forces and the direction of the pressure allows the C-ring to expand further into the sealing surface. Depending on the environment, HTSMAs could potentially be used in this application for pressure control, but more studies are presently being conducted to expand on this implementation. The experimental data and the modeling simulation that follows are novel for SMAs.

The setup used for the C-ring specimen is constructed by Aristotle University in Thessaloniki, Greece. As part of a research collaboration, the facility is available for testing thermomechanical SMA actuation using similar SMA testing techniques. Originally designed for variable loading corrosion - fatigue testing, the C-ring frame is reverted to apply constant loading using a vertical rod. A stainless steel rod fixes the C-ring in every direction except vertically. Only the forward transformation is considered due to the long heating and cooling time needed for reduction of temperature gradients. The temperature is increased using an induction heating chamber with padded insulation shown in Figure 23 and Figure 24. The temperature is measured using the thermocouple from the heating element, and from an external thermocouple used in the other setups discussed above. DIC is used to capture the strain field through a slit in the induction chamber.

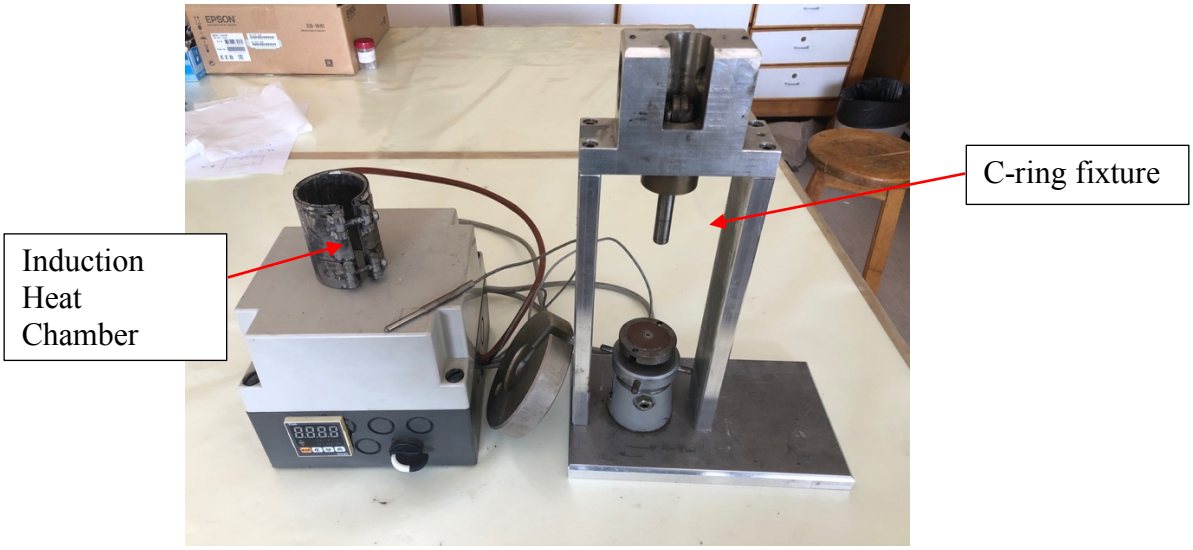

Figure 23 C-ring compression loading frame with an induction heater.

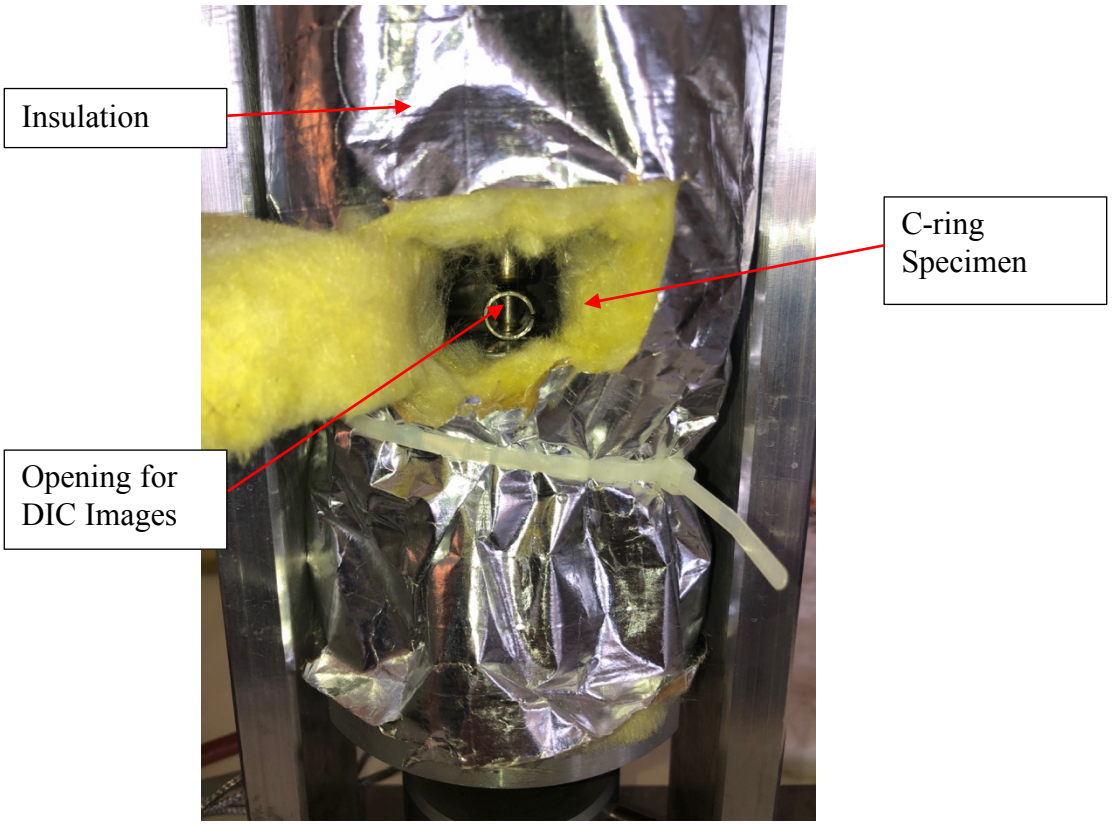

Figure 24 Thermal insulation chamber for C-ring actuation testing and view slit for DIC camera.

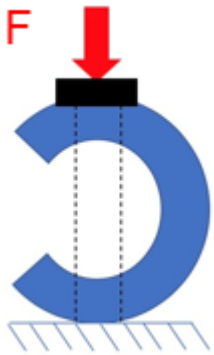

Figure 25 Schematic of loading condition for C-ring actuation testing.

3. EXPERIMENTAL RESULTS

3.1 Differential Scanning Calorimetry

The first step of the characterization process is running the DSC experiment on a small sample of the material. The latent heat release from the exothermic and endothermic phase transformation is captured to determine the phase transformation temperatures. Four DSC tests are run at the as received, solutionized, solutionized and heat treated, and only heat treated conditions, each for 3 cycles. The samples are vacuum sealed and water quenched if necessary for the treatment process. A selection is chosen based on stability and favorable transformation temperatures. Since the rod is hot extruded before being received, the best preparation option is the as received condition with a 550℃/3hrs heat treatment. This gives transformation temperatures M_f = 105 °C, M_s = 118 °C, A_s = 140 °C, and A_f = 155 °C.

DSC Test Matrix	
Heat Treatment	Temperature Rate
As received	10℃ / min
As received + Solutionized 950℃ / 1 hr	10℃ / min
As received + 550℃ / 3 hrs	10℃ / min
As received + Solutionized 950℃ / 1 hr + 550℃ / 3 hrs	10℃ / min

Table 1 Differential scanning calorimetry test matrix.

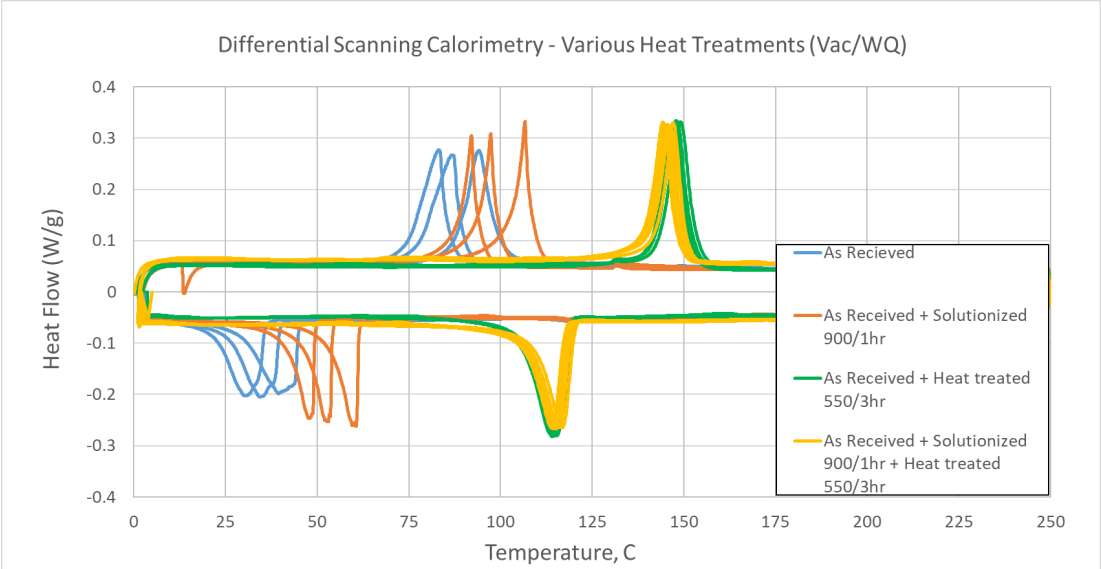

Figure 26 Differential scanning calorimetry for different heat treatments on the same HTSMA material.

3.2 Pseudoelastic and SME Response

Pseudoelastic tests are performed in order to get major material parameters. These tests are conducted on the MTS insight load frame discussed earlier in Section 2.3.5. The test is performed at a chamber stabilized temperature of 185℃, 30℃ above A_f, and loaded from 0N to 11,400N in crosshead control at a rate of 0.1mm/min for quasi static conditions. This material is not expected to provide a pseudoelastic response with the questionable purity, but 4.6% strain (out of the total 4.8%) is recovered upon unloading and the material clearly exhibits the pseudoelastic effect. The same test procedure is run in compression as well. The stress-induced transformation starts at 560MPa for the tension case, and 680MPa for the compression case. Compression

results show that there is no flat stress plateau and the martensite reorientation requires additional nominal stresses to complete detwinning.

A tension test to calculate the elastic modulus in the martensite phase is run as well, shown in Figure 28. The Shape Memory Effect occurs when the deformation caused in martensite is recovered after heating into the austenite phase in a stress-free condition. The test is performed at chamber stabilized 35℃, loaded from 0N to 4400N in crosshead control at a rate of 0.1mm/min for quasi static conditions. The test results in 1% strain at an average stress of 400MPa. The strain recovered from heating in a stress-free condition is 0.25%

Furthermore, a failure test in tension is performed. The failure stress is 1470MPa with an elongation of 7.6%. A brittle, transgranular cleavage fracture across a parallel plane perpendicular to the applied load is seen after the fracture. The large amount of energy absorbed is a result of the phase transformation and plastic deformation.

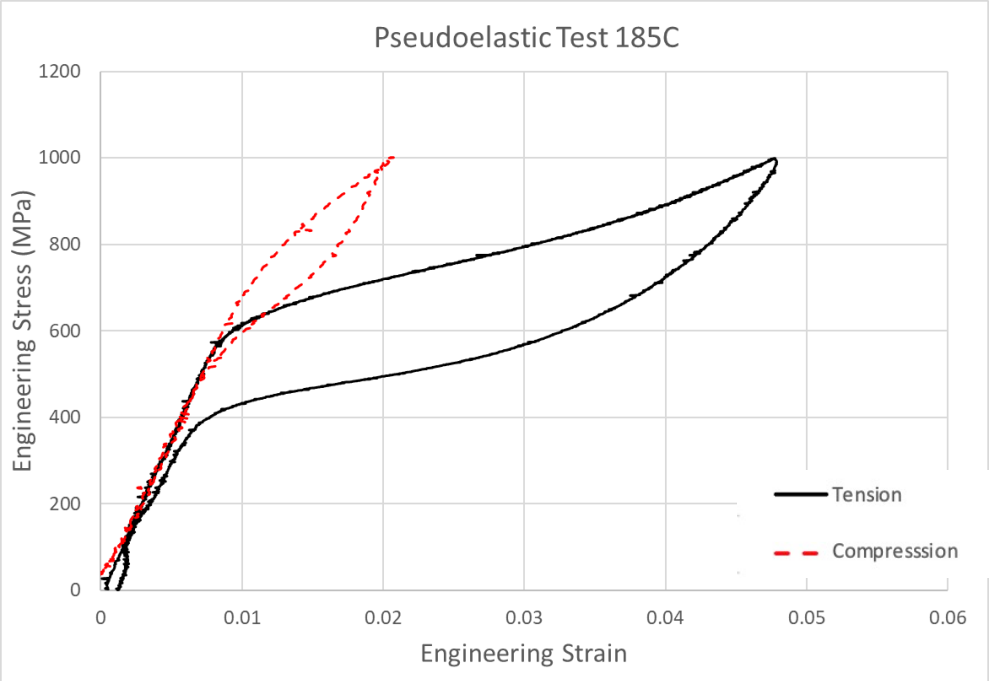

Figure 27 Pseudoelastic response in tension and compression.

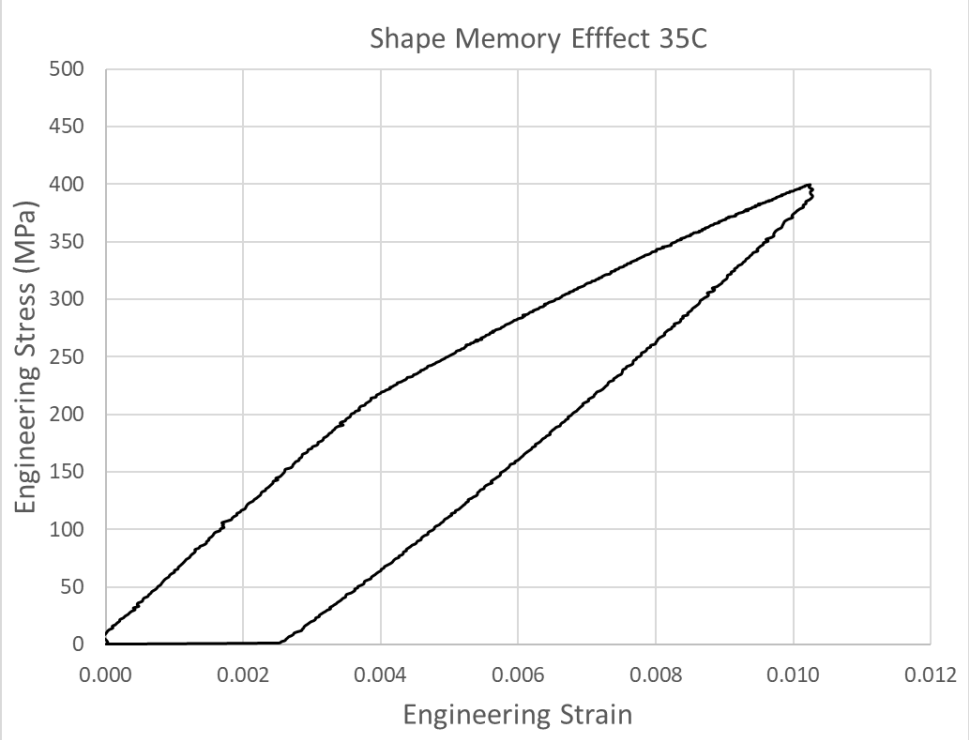

Figure 28 Shape Memory Effect in tension.

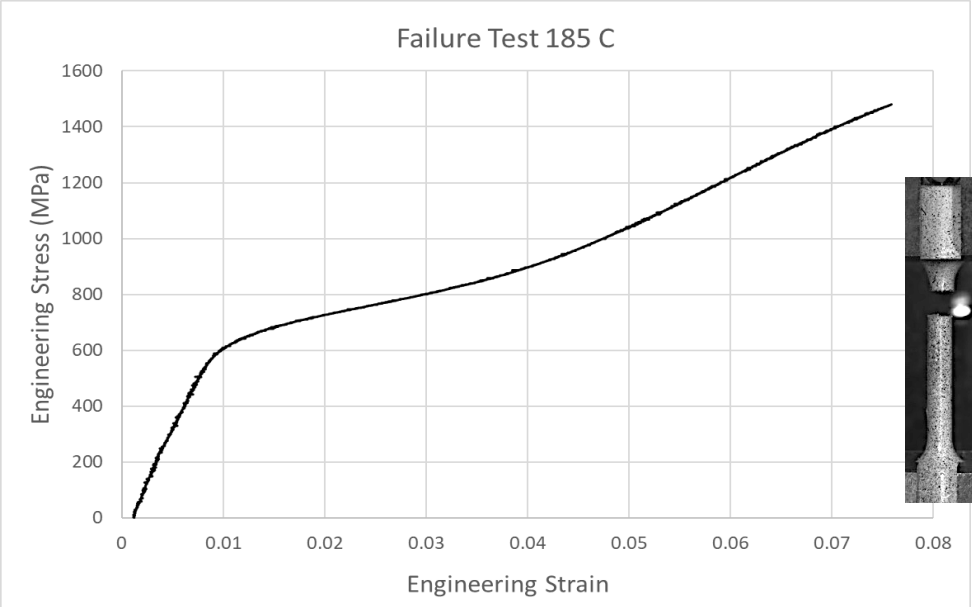

Figure 29 Failure response in tension.

3.3 Uniaxial Tension Actuation Cycling

Constant load actuation tests are run at average stress values of 50MPa, 100MPa, 150MPa, 200MPa, and 300MPa in order to characterize the thermomechanical response of the HTSMA. The joule heating is applied and controlled between a 35℃ lower cycle temperature and a 285℃ upper cycle temperature, which produces full transformation cycles. Each test is performed on a different specimen right after processing. The specimens are cycled enough for characterization and quantification of plastic strain.

Uniaxial Tension Actuation Test Matrix					
Specimen #	Cross Section Thickness, mm	Cross Section Width, mm	Gauge Length, mm	Stress, Mpa	Cycles
1	0.62	2.65	48.36	50	100
2	0.85	2.84	46.57	100	100
3	0.76	2.59	46.16	150	100
4	0.77	2.68	47.75	200	100
5	0.85	2.73	48.45	300	100

Table 2 Uniaxial actuation test matrix for each specimen tested.

The actuation hysteresis for each applied stress for the first cycle is shown in Figure 30. The transformation temperatures and the actuation strain increase with increasing applied load. Each set of transformation temperatures for each applied stress level is calculated using the method of tangents in order to create the phase diagram in tension [3].

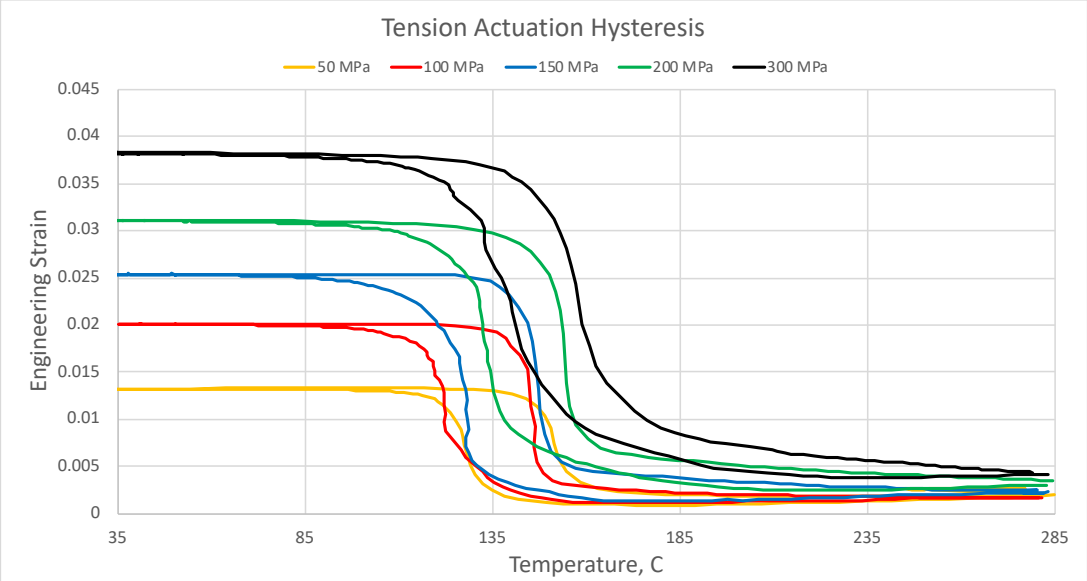

Figure 30 Actuation hysteresis for each stress level in the first cycle.

As shown in Figure 31, for each load magnitude, the total actuation strain remains constant throughout the thermomechanical actuation cycling and shows stability at least early in the fatigue life. Previous studies show that the actuation strain gradually decreases during the fatigue life due to softening and damage, but for the early fatigue life, it can be assumed constant [16, 36-37]. Furthermore, plastic strains develop after each subsequent cycle, shown in Figure 32. The TRIP strain development shows an expected trend with the applied stress levels, where increasing the applied load increases TRIP strain developed during cycling. The 50MPa test is not shown here due to data acquisition errors.

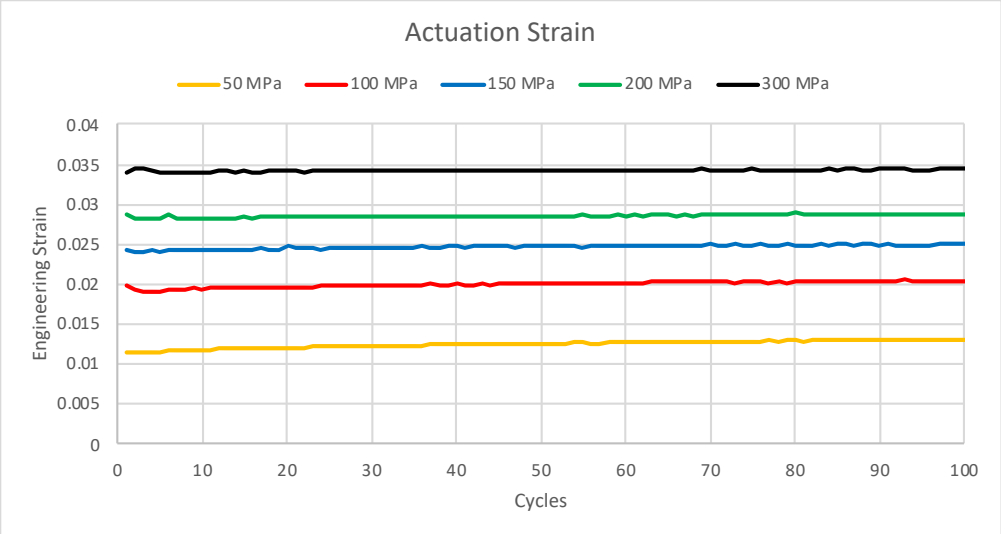

Figure 31 Actuation strain evolution for each stress level.

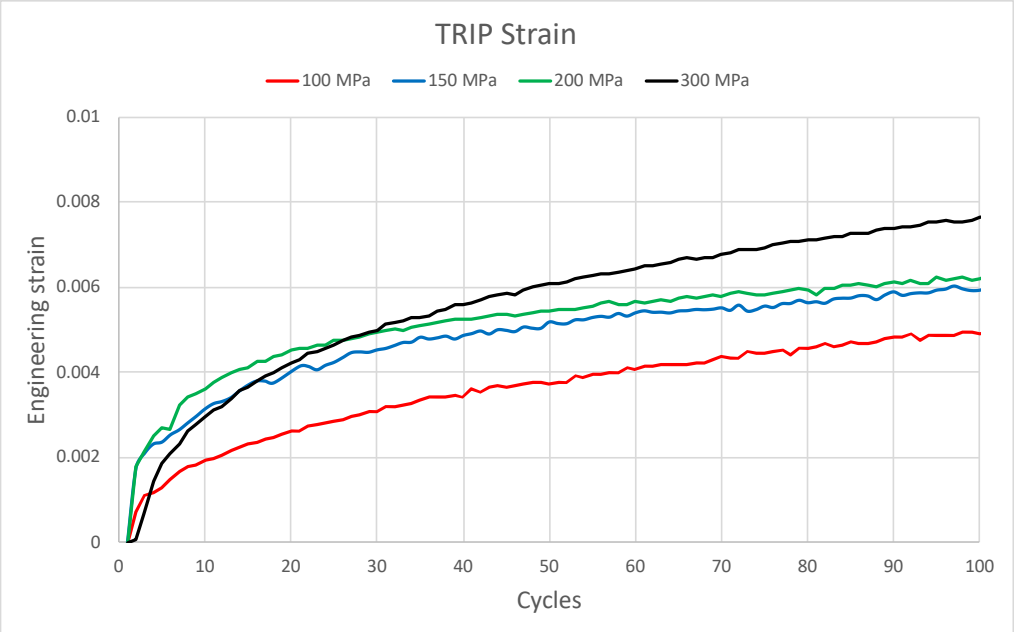

Figure 32 TRIP strain evolution for each stress level.

3.4 Internal Back Stress, TWSME

To characterize the TWSME, the parameters needed for internal back stress need to be determined. Tests are conducted to capture 100 constant load actuation cycles, under the same conditions and similar test specimens described above in Section 3.3, removing the load, and cycling 10 more time with only a small alignment load of 10MPa. This procedure is repeated to characterize the internal back stress throughout the cycling. No TWSME is obtained at 100MPa or 200MPa, training with 100 cycles. The internal back stress, in combination with the 10MPa alignment load had no macroscopic effect. TWSME might develop in this material, but much more thermomechanical cycling is required to move dislocations or pin martensite variants in the brittle material. For modeling of this material, the parameters responsible for TWSME will be set to

zero, although with more cycling, it is advised to reference data from other sources for full fatigue behavior of this material system [22, 46].

Two Way SME Test Matrix					
Specimen #	Cross Section Thickness, mm	Cross Section Width, mm	Gauge Length, mm	Stress, Mpa	Cycles
2	0.85	2.84	46.57	100 / 10	100 / 10
4	0.77	2.68	47.75	200 / 10	100 /10

Table 3 TWSME test matrix reusing test specimens from Section 3.3.

3.5 Tension - Compression Asymmetry

Three uniaxial, constant load actuation tests are performed in compression at similar nominal stress levels as in tension: 100MPa, 200MPa, 300MPa. The results comparing the first cycle of uniaxial tension is shown below for three of the stress levels. In general, the maximum transformation strain is significantly lower in compression, and the transformation temperatures are lower. High and low temperature regions where the thermal oven caused significant noise distortion for the DIC images are removed for clarity, but the data is sufficient for conclusions to be made and for modeling efforts. The transformation strain for each stress is quantified in Figure 36. There is about a 63% reduction in the transformation strain for the same applied stress in compression compared to tension. Measurements show the temperature on the specimen compared to the fixture temperature differed by around 9°C during cooling and heating, meaning there is a slight temperature gradient across the sample. The results shown in compression are influenced by the temperature gradient slightly, broadening the hysteresis and the

transformation temperature domain. The normalized compression data has been superimposed with the tension data to compare directly.

Uniaxial Compression Test Matrix		
Specimen #	Cross Section Area, mm	Stress Target, Mpa
6	11.44	100
7	11.40	200
8	11.42	300

Table 4 Uniaxial compression test matrix using cylindrical specimen.

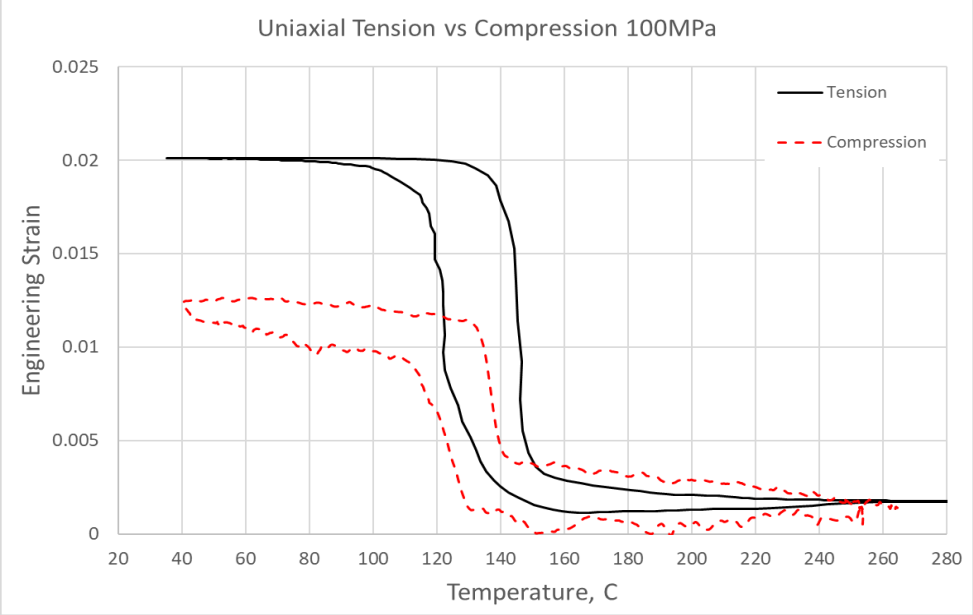

Figure 33 Constant load tension-compression asymmetry at 100MPa.

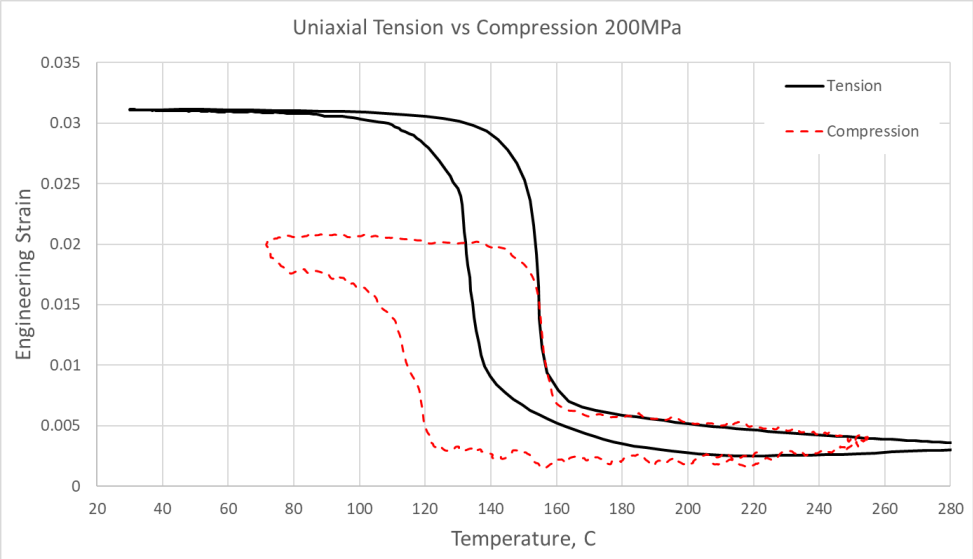

Figure 34 Constant load tension-compression asymmetry at 200MPa.

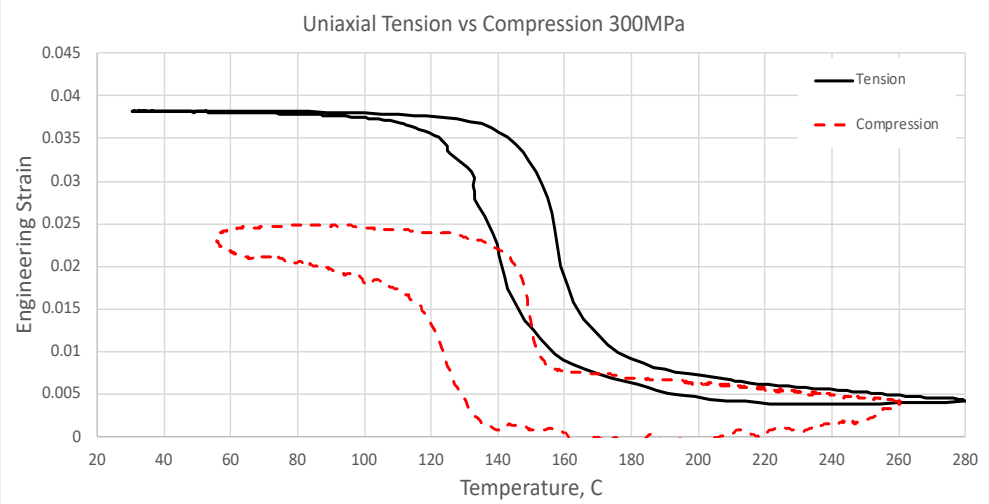

Figure 35 Constant load tension-compression asymmetry at 300MPa.

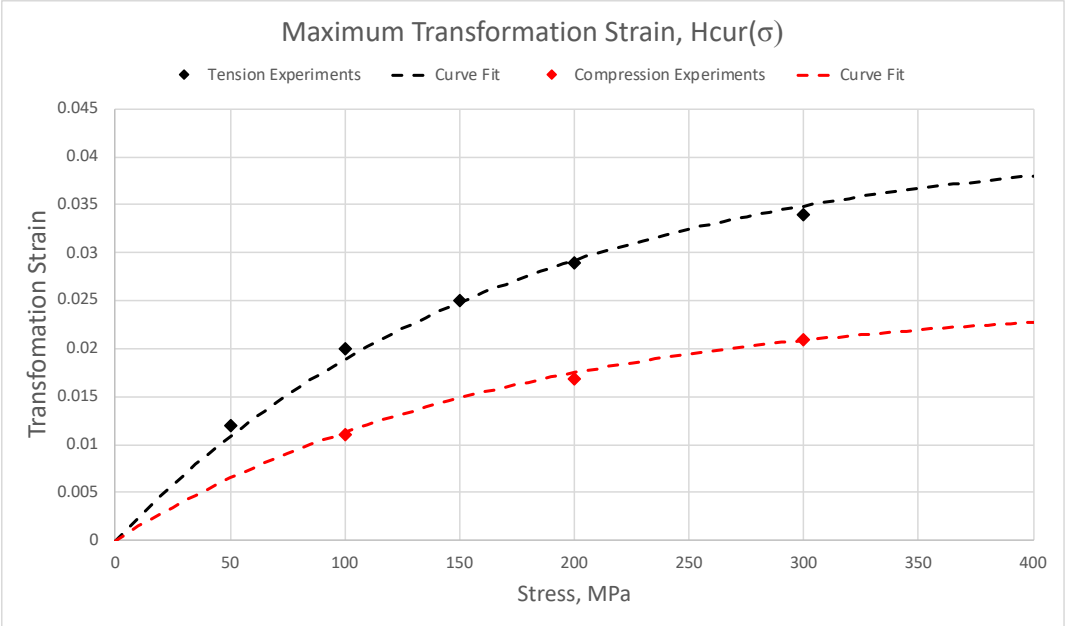

Figure 36 Maximum transformation strain from uniaxial tension tests at different constant load stresses.

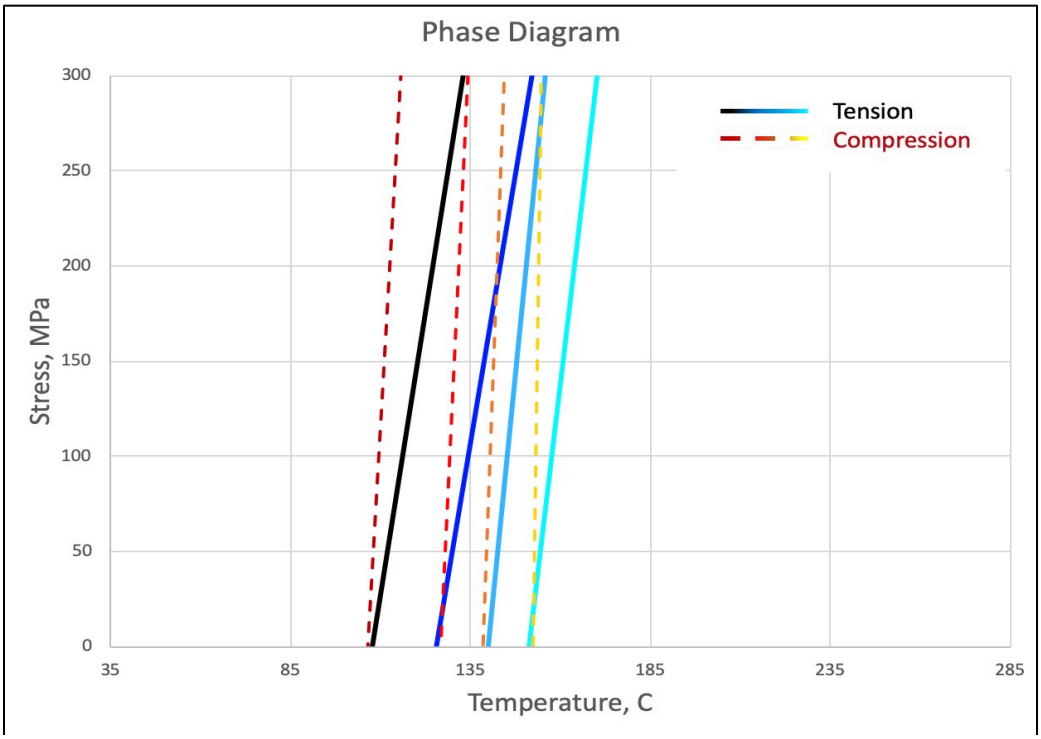

Figure 37 Phase diagram of the first actuation cycle in tension and compression.

3.6 Four Point Bending Actuation Result

The four point bending experiment consists of a constant 15.2N load, corresponding to a 40MPa flexural stress, and thermomechanically induced actuation cycling. Results show a significant displacement, up to 11mm at the midpoint, a maximum tensile strain of 0.8%, and a maximum compressive strain of 0.48% during forward phase transformation. The strain field at the midpoint section shows obvious strain asymmetry across the thickness in Figure 38 and Figure 41. Continued cycling results in an increase in vertical displacement after each subsequent cycle, as there is unrecovered deformation after each cycle.

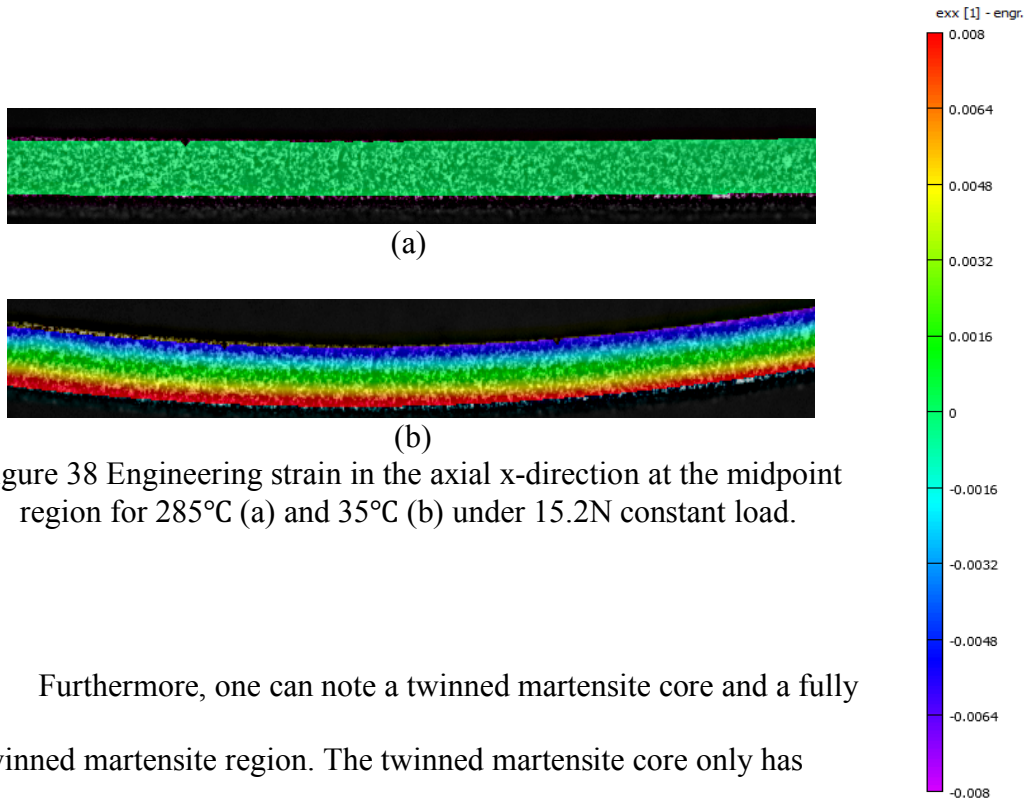

(a)

(b)

Figure 38 Engineering strain in the axial x-direction at the midpoint region for 285℃ (a) and 35℃ (b) under 15.2N constant load.

Furthermore, one can note a twinned martensite core and a fully detwinned martensite region. The twinned martensite core only has elastic and thermal strain contributions, while the detwinned region has strain contributions from thermomechanically induced phase transformation as well.

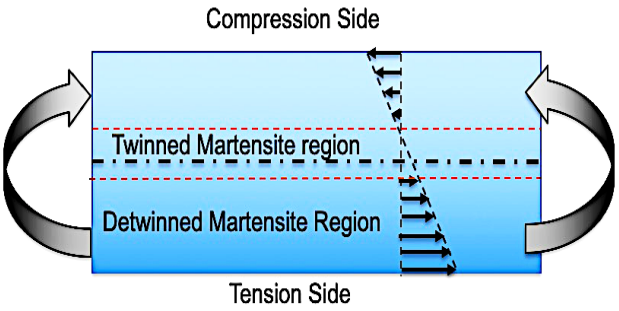

Figure 39 Schematic explaining strain response at low temperatures for constant load, thermomechanically induced phase transformation.

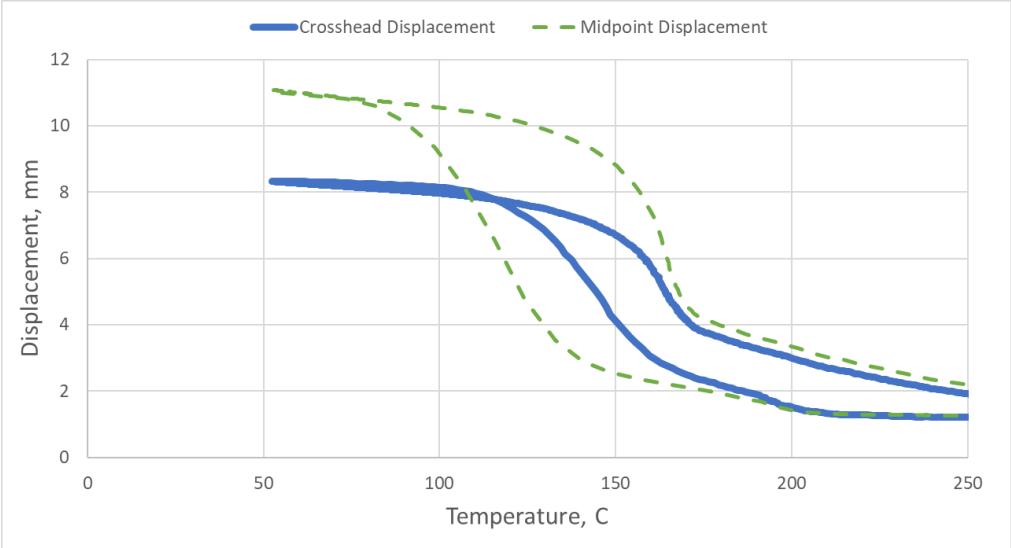

Figure 40 Four point bending displacement response at the crosshead and at the midpoint.

In order to show the tension-compression asymmetry across the thickness, four strain points are extracted from the DIC image at the midpoint where the maximum

displacement is recorded. The neutral axis location, where no axial strain is measured, is 0.2mm above the geometric center during forward phase transformation.

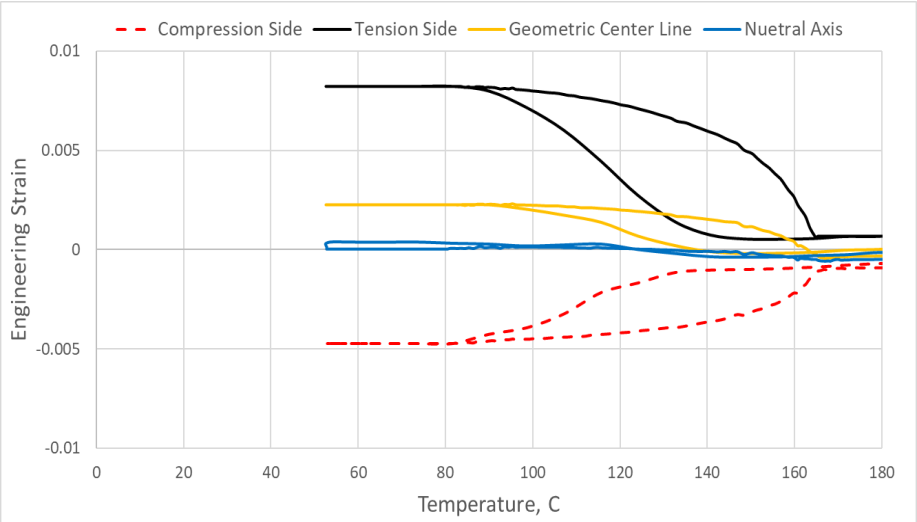

Figure 41 Localized engineering strain in the x-direction vs. temperature at the compression side, tension side, geometric center, and stress free neutral axis during the first cycle.

Furthermore, as cycling continued, the neutral axis continued to shift into the compression side at a similar rate as the TRIP strain. The relationship between the neutral axis shift and the plastic strain can be further understood by the summation of elastic, thermal, transformation, and plastic strains after a temperature cycle, where the only changes in strain is from plastic strain. A clear relationship is shown by Figure 42 where the transformation induced plastic strain at the bottom of the plate and neutral axis differ only by a scalar.

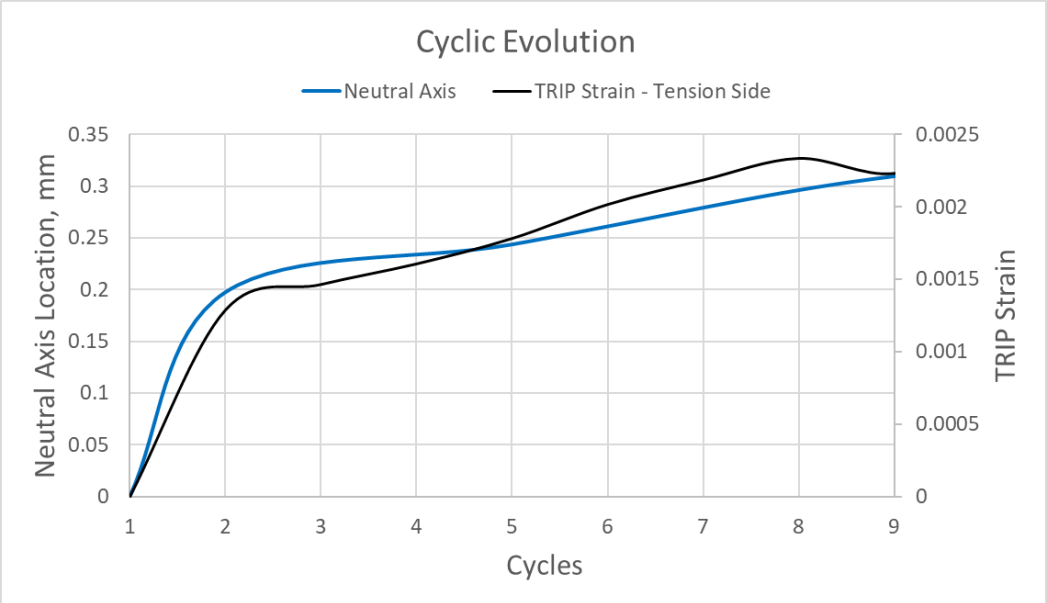

Figure 42 Neutral axis shift and TRIP strains on the tension side superimposed after 9 thermomechanical cycles.

3.7 C-ring actuation results

The C-ring is loaded in compression along the center vertical axis with 266N. The thermal induction chamber starts at 285℃ and is then cooled to 35℃ by the surrounding air. The first reference image is collected after loading; Figure 43 shows the strain contributions from phase transformation and thermal expansion only, without any elastic contributions. The DIC data shows engineering maximum principal strains in a global Cartesian coordinate system (polar coordinate transformations are not possible using the Vic-2D software). During cooling, the phase transformation occurred in tension, followed by phase transformation in compression.

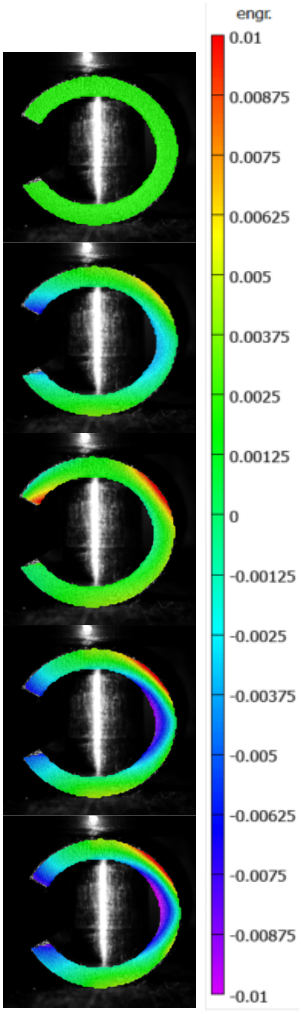

Figure 43 Max principal strain from C-ring thermomechanical actuation test.

The measured principal strain at the tips of the C-ring is most likely from measurement error due to the speckle pattern and minor lighting issues on the left half of the image. Lastly, the DIC results are expected to be symmetric about the horizontal plane of symmetry in the middle of the C-ring; the test results could be influenced by a slightly eccentric load, material impurity, or inaccurate machining of the test specimen.

4. MODELING IMPLEMENTATION

4.1 Modeling of SMAs

Two macromechanical model methodologies are used to simulate the phase transformation in polycrystalline SMAs. One methodology uses single crystal or single grain properties averaged over a representative volume element, while the other uses a macro free energy potential derived from micromechanical modeling [48]. The motivation of this research is so develop and validate the latter; a macroscale model based on Gibbs free energy. Here, the volume fraction of martensite is used as an internal state variable along with a transformation evolution equation to relate to the transformation strain. The forward transformation is described with a transformation surface, which describes the boundary of the thermoelastic domain [49]; more detail on the transformation surface will be discussed in Section 4.1.2. The model is extended further by the work of Lagoudas and Entchev where more state variables are introduced: transformation strain, plastic strain, drag stress, and back stress [49-50] to account for cycling and thermomechanical actuation phenomena. Introduced below are the model frameworks from Xu *et al*. to capture TRIP and the internal back stress [1], and from Hartl *et al*. to capture anisotropy in SMA phase transformation [2]. Both models are needed to match the experimental results shown in Section 3.

4.1.1 Thermomechanical Potential and Constitutive Equations

The Gibbs free energy, G, is a continuous function dependent on the Cauchy stress tensor σ, temperature T, and a set of internal state variables $\Upsilon = \{\varepsilon^t, \varepsilon^p, \beta, \xi\}$, the transformation strain tensor ε^t, the TRIP strain tensor ε^p, the internal stress tensor β,

and the martensitic volume fraction scalar ξ. The additional terms, ε^p and β, are added by Xu *et al*. to capture transformation induced plasticity and the two way shape memory effect [1]. Without ε^p and β, one recovers the thermomechanical potential used by Hartl *et al*. [2].

$$G = -\frac{1}{2\rho}\boldsymbol{\sigma} : \mathcal{S}\boldsymbol{\sigma} - \frac{1}{\rho}\boldsymbol{\sigma} : [\,\boldsymbol{\alpha}(T - T_0) + \boldsymbol{\varepsilon}^t + \boldsymbol{\varepsilon}^p] - \frac{1}{\rho}\int_0^{\xi}(\boldsymbol{\beta} : \frac{\partial \boldsymbol{\varepsilon}^t}{\partial \xi})d\xi + c\Big[(T - T_0) - T\ln(\frac{T}{T_0})\Big] - s_0 T + u_0 + f(\xi)$$

S is the effective fourth-order compliance tensor, α is the effective second order thermal expansion tensor, c is the effective specific heat, s_0 is the effective specific entropy, μ_0 is the effective specific internal energy, and $f(\xi)$ is the smooth hardening function.

$$\mathcal{S}(\xi) = \mathcal{S}^A + \xi(\mathcal{S}^M - \mathcal{S}^A) = \mathcal{S}^A + \xi\Delta\mathcal{S}$$

Following thermodynamic principles and Coleman-Noll procedure, the constitutive relationship can be expressed as:

$$\boldsymbol{\varepsilon} = -\rho\frac{\partial G}{\partial \boldsymbol{\sigma}} = \mathcal{S}\boldsymbol{\sigma} + \boldsymbol{\alpha}(T - T_0) + \boldsymbol{\varepsilon}^t + \boldsymbol{\varepsilon}^p$$

$$s = -\rho_0\frac{\partial G}{\partial T} = \frac{1}{\rho}\boldsymbol{\sigma} : \boldsymbol{\alpha} + c\ln(\frac{T}{T_0}) - s_0$$

The smooth hardening function, $f(\xi)$, accounts for the hardening effects associated with the transformation process. Intermediate parameters, a_1, a_2, and a_3, along with curve fitting parameters, n_1, n_2, n_3, and n4 are introduced to satisfy smooth transition behaviors [1].

$$f(\xi) = \begin{cases} \frac{1}{2}a_1\left(\xi + \frac{\xi^{n_1+1}}{n_1+1} + \frac{(1-\xi)^{n_2+1}}{n_2+1}\right) + a_3\xi \ , \ \dot{\xi} > 0, \\ \frac{1}{2}a_2\left(\xi + \frac{\xi^{n_3+1}}{n_3+1} + \frac{(1-\xi)^{n_4+1}}{n_4+1}\right) - a_3\xi \ , \ \dot{\xi} < 0 \end{cases}$$

4.1.2 Transformation Functions

There are more formulations of the Gibbs free energy framework based on different transformation surfaces, J_2, J_2 - I_1 and the generalized J_2 - J_3 - I_1. In short, J_2 based transformation functions cannot capture tension–compression asymmetry; J_2 - I1 based transformation functions can capture tension-compression asymmetry or pressure dependence; J_2 - J_3 - I_1 based transformation functions capture volumetric transformation strain, asymmetry, and pressure dependence [48]. Simulations using a J_2 and a specialized J_2-J_3 transformation function is shown in Section 4. The specific derivations using the two different transformation surfaces is extensive, and the author advises to reference the publications that implement the transformation surfaces directly for more details [1-2, 48].

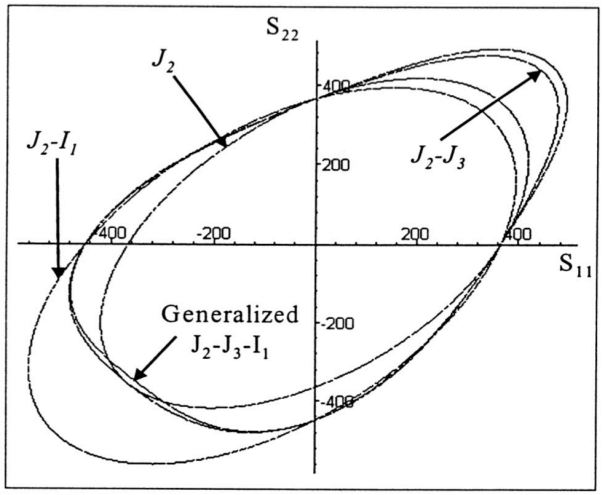

Figure 44 Plot of J2, J2 – I1, and J2 – J3 – I1 transformation function in S11 - S22 space reprinted from [48].

The first phenomenological, macroscopic constitutive SMA model used to simulate the thermomechanical actuation cycling in this study is based on the recent work by Xu, *et al*. [1]. It is a J_2 based transformation function and currently cannot capture asymmetric behaviors. It does, however, incorporate TRIP, internal back stress, and smooth hardening functions. The other phenomenological, macroscopic constitutive SMA model used for anisotropy is based on the work by Hartl, *et al*. [2]. The specific purpose of the study by Hartl *et al*. is to generalize and capture inelastic single crystal response with anisotropic yield surfaces for SMAs, capturing micromechanical response in a computationally efficient way. It represents orthotropic generalizations of the classical J_2-J_3-I_1 transformation function, and can capture tension-compression asymmetry and pressure dependence in shape memory alloy forward phase transformation with slight modifications. The generalized J_2-J_3-I_1 transformation

function can be simplified to obtain the J_2-J_3 transformation function by making the generalization parameters (a_{ax}, a_{shr}, b_{ax}, b_{shr}, b_{11}) in $J_2^O \; and \; J_3^O$, equal to 1.0, and calibrating c to match the experimental tension-compression asymmetry [2].

$$\hat{\Phi}(\mathbf{S}) := \eta\sqrt{3J_2}\left[1 + \upsilon\frac{J_3}{(3J_2)^{\frac{3}{2}}}\right]^{\zeta} + \omega I_1$$

When,

$$\eta = H\ , \zeta = \tfrac{1}{3}, \omega = 0, \upsilon = -3^{\frac{3}{2}}c$$

$$\hat{\Phi}_{fwd}(\boldsymbol{\sigma}) = H\hat{\bar{\Phi}}_{fwd}(\boldsymbol{\sigma}) = H\sqrt{3}\left[(J_2^O)^{\frac{3}{2}} - cJ_3^O\right]^{1/3}$$

4.1.3 Abaqus UMAT Implementation

Both models have been implemented into a user-defined material subroutine (UMAT) under the commercially available finite element software, Abaqus. The implementation into a well-established structural analysis software functions as an important design tool that allows for simulation or optimization of the macroscopic response of SMAs. The inputs to these models are determined based on experiments and the phenomenological response. The method to calculate the parameter inputs is discussed in the next Section. There are some discrepancies between the model inputs, such as anisotropy or TRIP but the major material parameters and the smooth hardening parameters are the same.

ABAQUS allows for simulation of the experiments. Models for the plate and C-ring geometries are made in the ABAQUS interface and the boundary conditions are

applied. The accuracy of each model can be compared with the experiments. Future work, discussed in Section 4.5, briefly outlines improvements to anisotropy, TRIP evolution, and maximum transformation strain equations.

4.2 Model Characterization

The characterization procedure for an SMA material is much more involved than a typical metallic material. In addition to the standard material properties, usually defined by the Metallic Materials Properties Development and Standardization (MMPDS) for aerospace applications, SMAs require experimental data describing the phase transformation temperatures, smooth hardening parameters in tension and compression, and cyclic evolution. [51-52].

4.2.1 Differential Scanning Calorimetry

Differential Scanning Calorimetry, or DSC, is important for the characterization and classification of SMAs. It is used to determine the transformation temperature range of the material at zero applied load. Since the transformation from austenite to martensite is dependent on the release and absorption of latent heat, DSC can capture the phase transformation temperatures, latent heat during transformation, and specific heat capacities of different phases by quantifying the change of heat flow to the SMA. A typical DSC curve is shown below in Figure 45 [3]. The test provides the transformation temperatures: M^f, M^s, A^s, A^f, the specific heats: c^A, c^M, as well as $\rho\Delta s0$. The transformation temperatures and specific heats are extrapolated directly, but the other parameters need to be calculated. $\rho\Delta s0$, the change in the specific entropy per unit volume, is found using the average forward and reverse transformation temperatures, T^f

and T^r, the area of the latent heat absorption and release on a normalized heat flow scale (W/g), and the applied temperature rate, T'.

$$\rho\Delta s0 = \frac{2*Qex_f}{Tr+Tf} \qquad Qex_f * T' = \int_{Mf}^{Ms} Q'\,dT$$

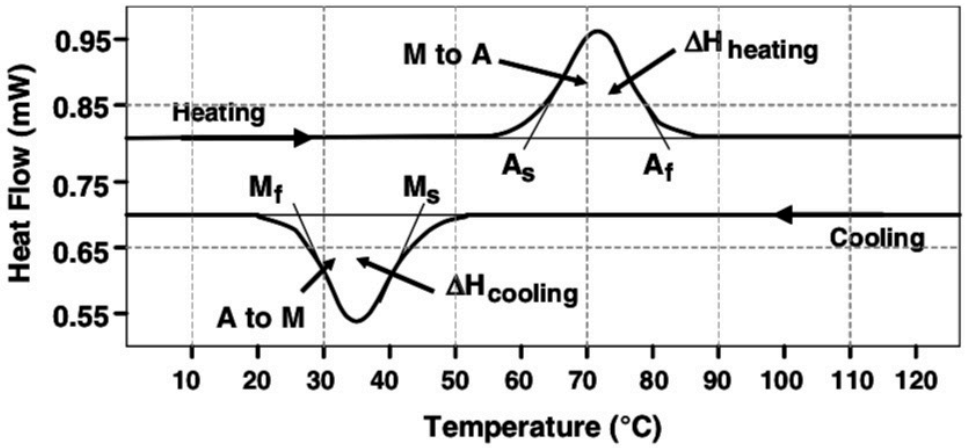

Figure 45 DSC schematic showing the latent heat of phase transformations and the corresponding transformation temperature reprinted from [3].

4.2.2 Major Material, Smooth Hardening, Evolution Parameters

E^A and E^M can be calculated by taking the slopes of the stress-strain curve from uniaxial tension loading above the A^f temperature as shown in Figure 46(a). Since some SMA material systems do not exhibit a second martensite slope, the Elastic Modulus in martensite can be calculated from a uniaxial tension test at a temperature below M^s shown in Figure 46(b).

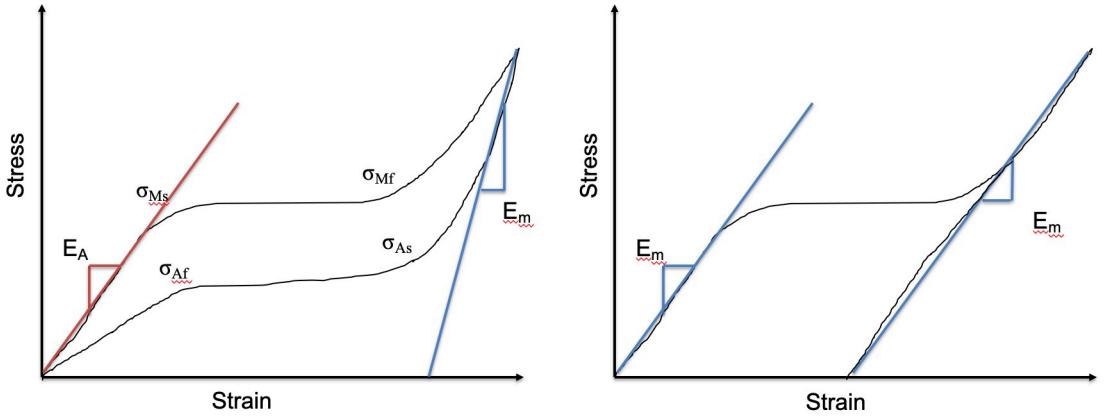

(a) (b)

Figure 46 Uniaxial tension tests at a constant temperature above Af (a) and below Ms (b).

The tensile actuation tests provide the phase diagram constants: C^A, C^M, the smooth hardening parameters: Hmax, k^t, n1, n2, n3, n4, and the evolution Parameters after cycling: σ^b, C_1^P, C_2^P, λ_1.

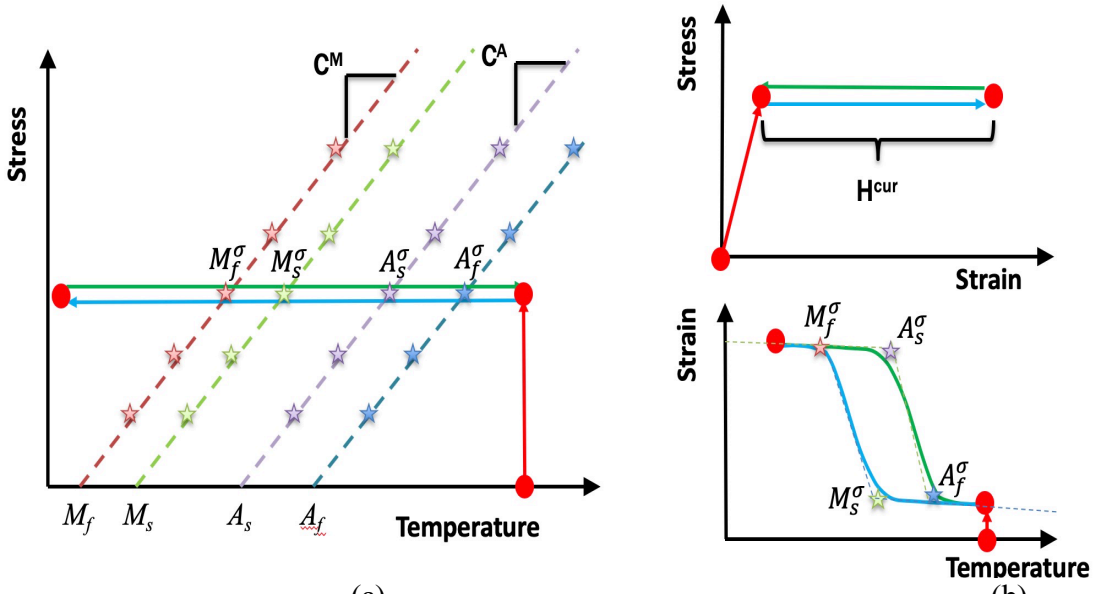

(a) (b)

Figure 47 Phase diagram of the SMA (a) after five thermomecanical loading paths (b) and the calibration parameters.

The maximum transformation strain, Hcur, is depenent on the applied stress level in constant load loading conditions. Hmax and k^t describe the change in the maximum transformation strain using:

$$H^{cur}(\boldsymbol{\sigma}) = H^{max}(1 - e^{-k_t \bar{\boldsymbol{\sigma}}_f})$$

The smooth hardening parameters n1, n2, n3, n4 are determined by matching the hysteresis evolution corners with a smooth transition [1].

The evolution parameters are determined by fitting curves to experimental data consisting of TRIP and TWSME. The current TRIP model uses C_1^P, C_2^P to describe an exponential curve based on the maximum saturation strain [3]:

$$\varepsilon^p = C_1^p C_2^p \left(1 - e^{-\frac{\zeta^d}{C_2^p}}\right) = \varepsilon_{\text{sat}}^p \left(1 - e^{-\frac{\zeta^d}{C_2^p}}\right)$$

Updated parameters using a logarithmic function, dependent on stress, is discussed in Section 4.5. σ^b and λ_1 describe the TWSME phenomenon and the internal stresses formed from thermomechanical cycling1. The effective stress is an addition of the externally applied stress and the internal stress, β:

$$\boldsymbol{\beta} = \sigma_b \frac{\boldsymbol{\sigma}_f}{\bar{\boldsymbol{\sigma}}_f}(1 - e^{-\lambda_1 \zeta^d})$$

4.3 Characterization Results

The experiments in Section 3 provide the full characterization of the SMA for both ABAQUS UMATs. The calibration parameters used for the J_2 based transformation

function model is shown in Table 5. Table 6 shows additional terms that capture tension - compression asymmetry.

Type	Parameter	Value [Unit]	Parameter	Value [Unit]
Major Material Parameters (13)	E_A	70 [GPa]	C_A	17.33 [MPa/K]
	E_M	48.7 [GPa]	C_M	11.51 [MPa/K]
	ν_A, ν_M	0.3	M_s	398 [K]
	α_A, α_M	1.30E-05	M_f	378 [K]
	ρ	0.00855 [g/mm^3]	A_s	413 [K]
	c_A, c_M	0.302 [J/gK]	A_f	428 [K]
	$\rho\Delta s0$	- 0.3118 [MJ^3K]		
Smooth Hardening Paramters (6)	H_{max}	0.0405	n_2	0.88
	k_t	0.00585	n3	0.001
	n_1	0.88	n4	0.001
TRIP and Internal Stress Parameters (4)	σ_b	0 [MPa]	λ_1	0.1
	C_{1P}	0.000605	C_{2P}	15

Table 5 Calibration parameters for current J2 based transformation function model.

Type	Parameter	Value [Unit]	Parameter	Value [Unit]
Major Material Parameters (13)	E_A	70 [GPa]	C_A	17.33 [MPa/K]
	E_M	48.7 [GPa]	C_M	11.51 [MPa/K]
	ν_A, ν_M	0.3	M_s	398 [K]
	α_A, α_M	1.30E-05	M_f	378 [K]
	ρ	0.00855 [g/mm^3]	A_s	413 [K]
	c_A, c_M	0.302 [J/gK]	A_f	428 [K]
	$\rho\Delta s0$	- 0.3118 [MJ^3K]		
Smooth Hardening Paramters (6)	H_{max}	0.0405	n_2	0.88
	k_t	0.00585	n3	0.001
	n_1	0.88	n4	0.001
Assymetry Parameters (6)	a_{ax}	1.0	b_{ax}	1.0
	a_{sr}	1.0	b_{sr}	1.0
	c	-1.82	b_{11}	1.0

Table 6 Calibration parameters for current J2-J3 based transformation function model.

In order to confirm the calibration results from the experimental data, a computationally efficient Matlab code is used to represent a 1-D SMA constitutive model. The Matlab code shows good agreement between the uniaxial tensile actuation experiments using the values from Table 5. This does not capture asymmetry, but the

results are important for the smooth hardening parameters that are used for actuation cycling.

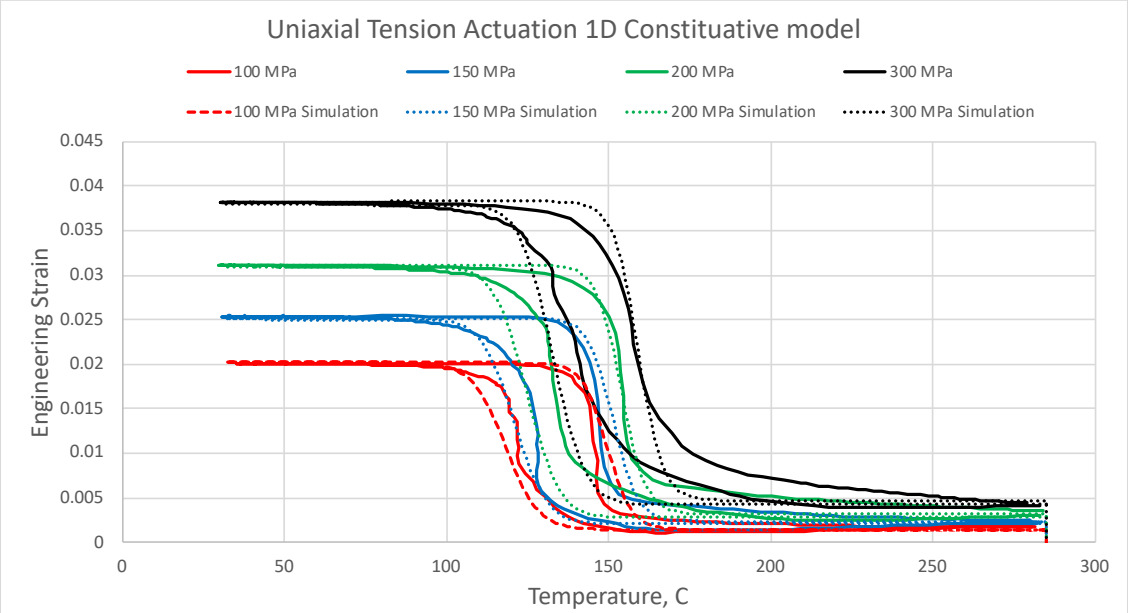

Figure 48 Uniaxial tension actuation results comparing experimental data to 1D simulations.

For the calibration of the J_2-J_3 invariant model, a looping algorithm determines the asymmetry parameter c in Table 6 by running a single element, periodic FEA model under a uniaxial thermomechanical loading path. Each run calculated the error between the simulated and measured transformation strain for tension and compression under 300 MPa, 200 MPa, and 100 MPa. The error is minimized until a final result for the asymmetry parameter, c, is determined. The results are shown in Figure 49; the simulation and experimental data agree fairly well by using c = -1.82.

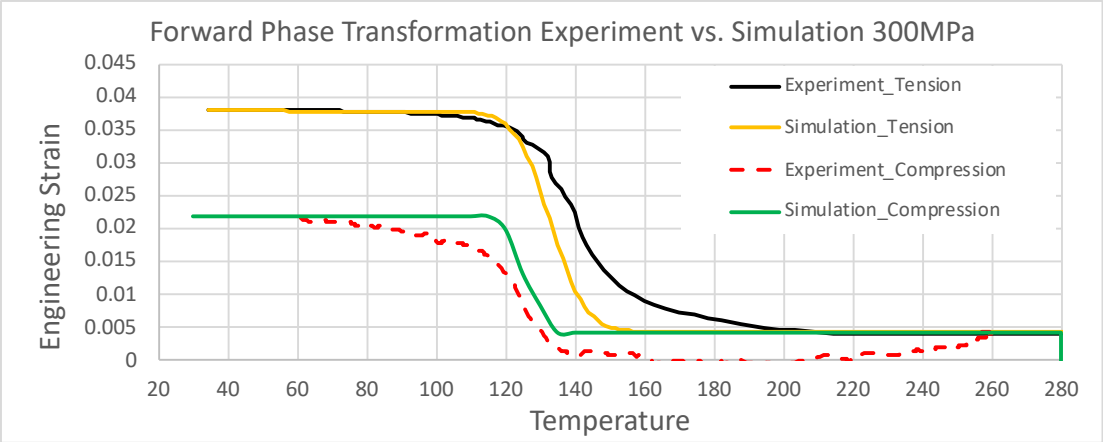

(a)

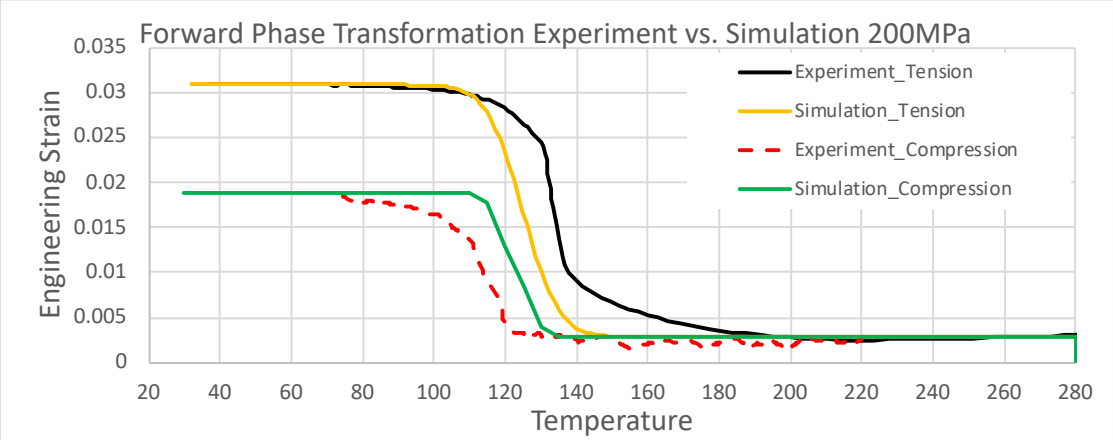

(b)

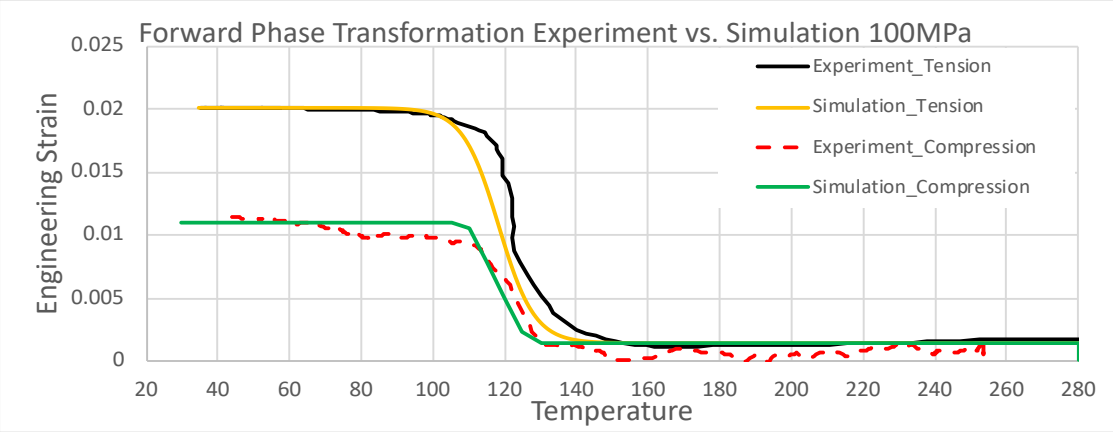

(c)

Figure 49 Forward phase transformation comparison between experiment and simulation showing that the parameters from Table 6 provide accurate simulations of tension - compression asymmetry. 300MPa (a), 200MPa (b), 100MPa (c).

4.4 Pure Bending and C-ring Simulations

4.4.1 Four Point Bending Simulation (J2 and J2-J3)

The experiments provided allow for validation of the ABAQUS UMAT implementations of the SMA constitutive model for the two different phase transformation surfaces. The simulation provides a modeling attempt that shows that the current ABAQUS UMAT can capture the experiments fairly closely.

The 3D FEA model designed matches the specimen dimensions, and the boundary conditions that related to the 4 point experimental setup. It consists of $1/4^{th}$ of the total structure with x and y periodicity to represent symmetry along the length and width to reduce computational effort. The mesh is converged using quadratic tetrahedral elements (C3D10M) with 12.6 k degrees of freedom. Each temperature cycle takes 362 seconds of CPU time with an Intel® Core™ i7-4770 with 3.40GHz and 32.0GB installed memory on Abaqus 6.14.

The simulation matches the experiment displacement and strain relatively closely through the thermomechanical cycling. Without tension - compression asymmetry implemented in the UMAT simulation, as expected, the maximum compression strain is over predicted. As a consequence, the plastic strain developed in the tension side is under predicted, and the plastic strain in the compression side is over predicted. This results shows that the model is capable of capturing the cyclic response of the HTSMA beam once the improvements to asymmetry are completed.

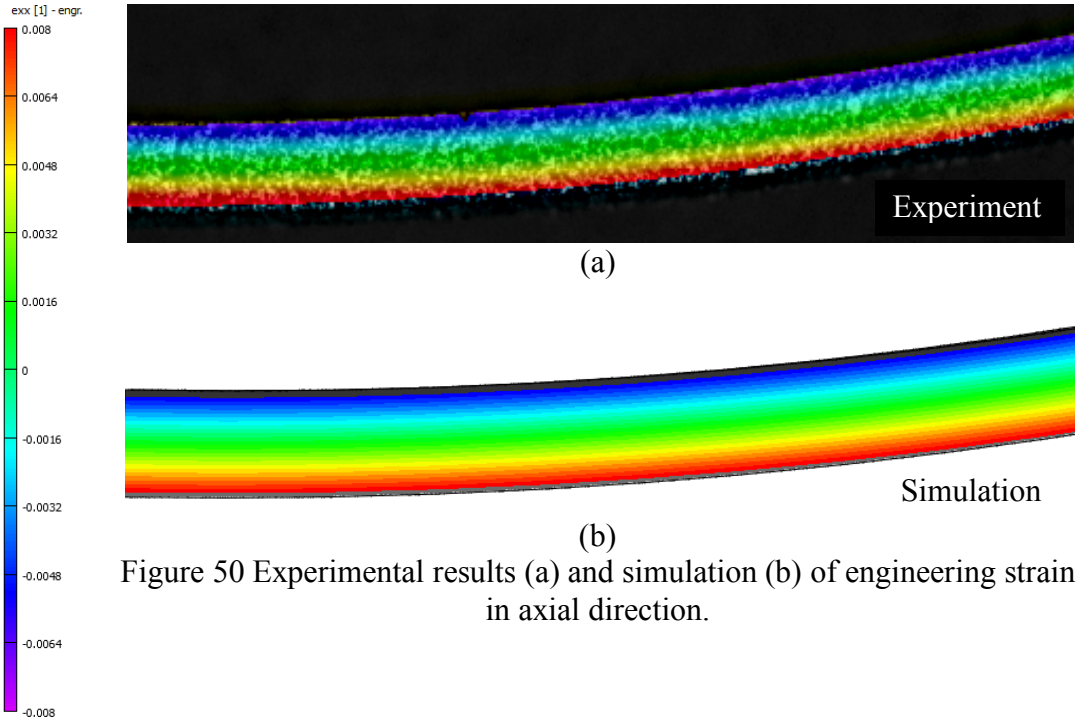

Figure 50 Experimental results (a) and simulation (b) of engineering strain in axial direction.

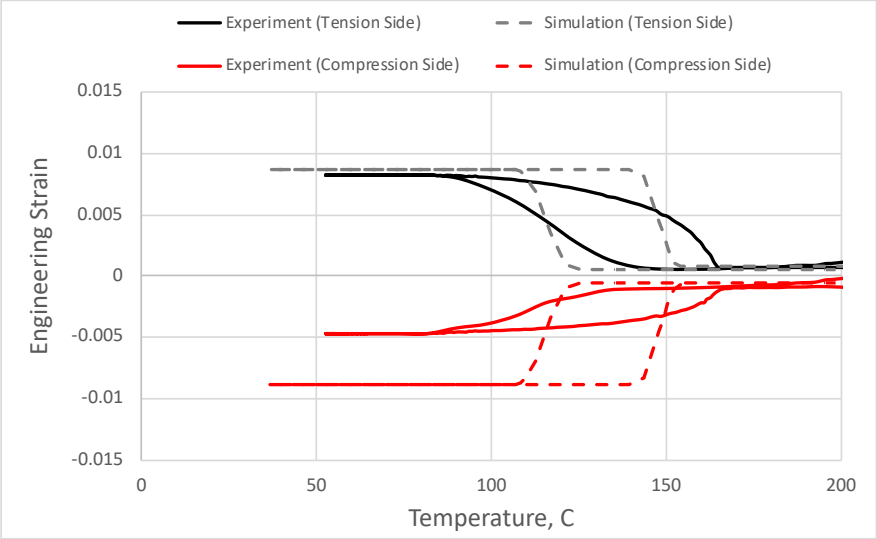

Figure 51 Simulation and experimental results comparison of four point bending test showing the engineering strain at the top (Compression side) and bottom (Tension Side) at the midpoint.

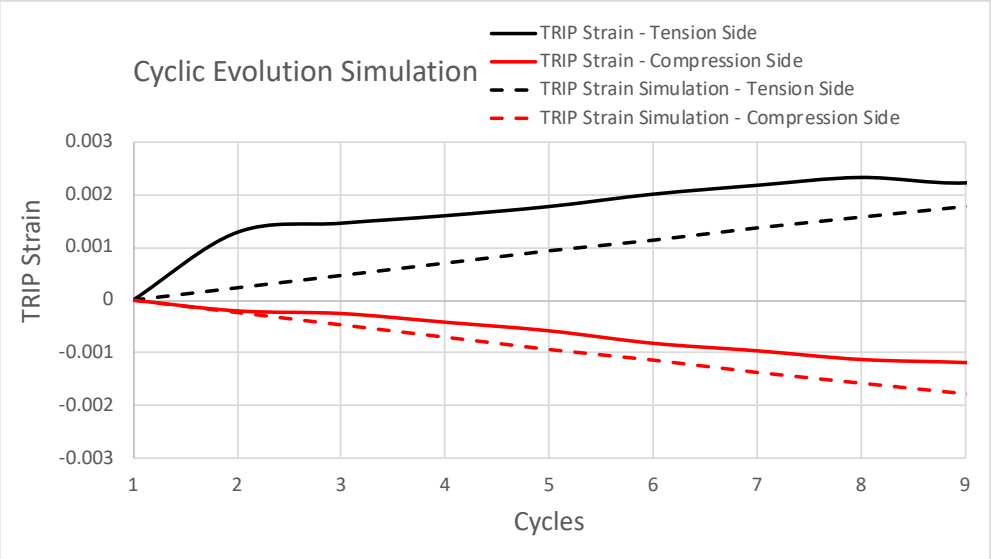

Figure 52 Unrecovered strain after thermal cycling in four point bending.

The same bending model above is again used with the parameter set in Table 6. The only differences is the parameters used for the asymmetry and only simulating forward phase transformation; the mesh, load, and boundary conditions are all the same. There is good correlation between the experimental results and the anisotropy simulation using the J_2-J_3 transformation surface and the simulation accurately captures the macroscopic response during forward phase transformation. The neutral axis shift is also captured and can be seen by plotting the strain at the geometric center for the simulation and the experiment.

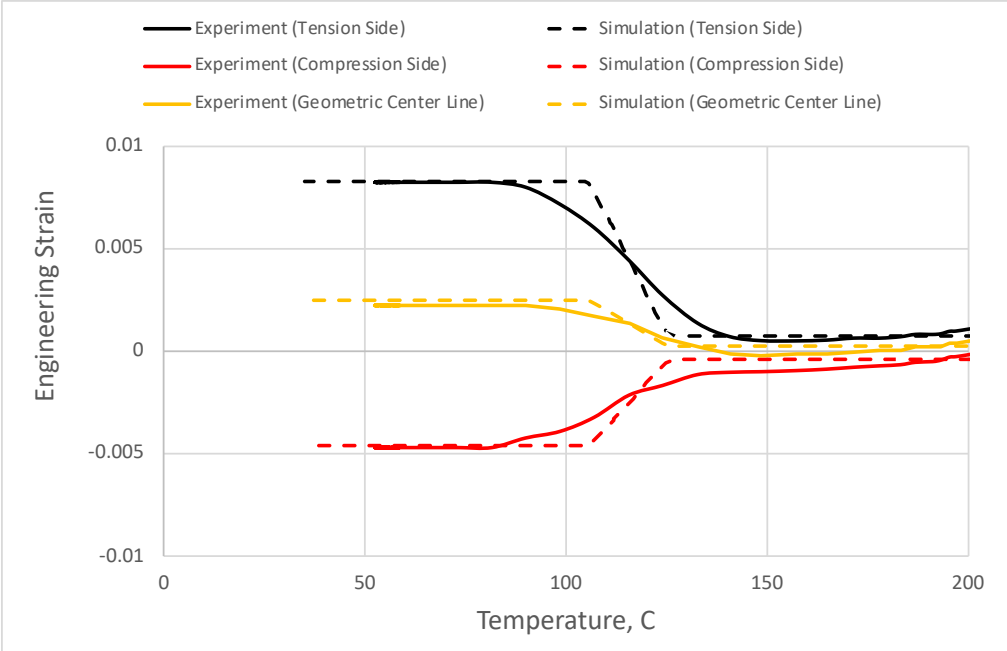

Figure 53 Forward Phase transformation comparison between experiment and simulation showing asymmetry in the bending response and a neutral axis shift at the geometric center.

4.4.2 C-ring Simulation (J_2-J_3)

Similar to the bending plate model, a 3D FEA model of the C-ring geometry is created in ABAQUS. The purpose of this simulation is to match experiment results and validate the tension-compression asymmetry using a complex, multi-axial thermomechanical loading path. The geometry, boundary conditions, and parameters from Table 6 are used to simulate the experiment. The load is placed on a reference point with a beam type MPC constraint that connected elements within the area of the applied load; granted this is not the best way to model the load application, but since the area of interest is far away from the load point, it is assumed to be a good approximation. The mesh is converged using quadratic tetrahedral elements (C3D10M) with 271.6 k degrees

of freedom. A run take 321 seconds of CPU time with an Intel® Core™ i7-4770 with 3.40GHz and 32.0GB installed memory on ABAQUS 6.14.

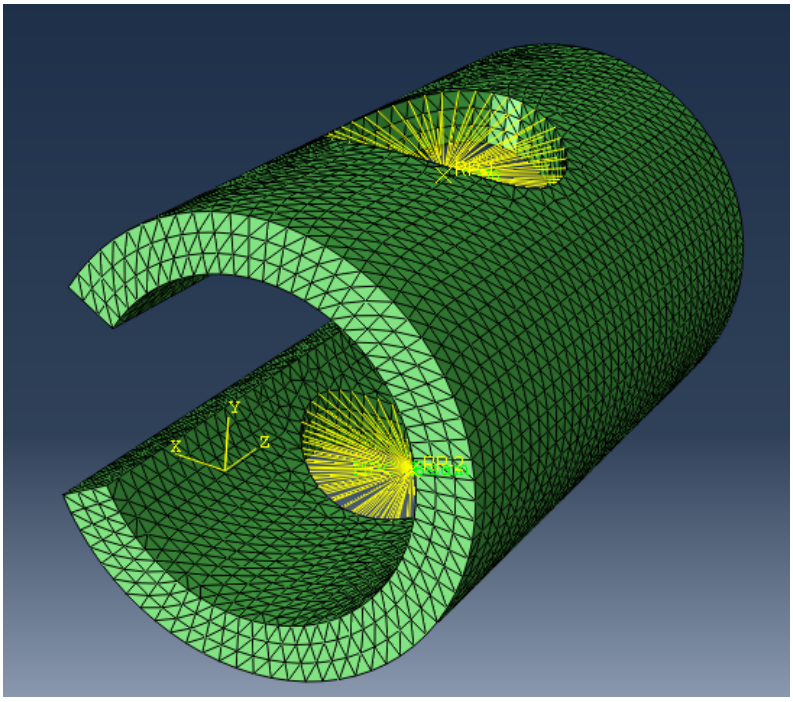

Figure 54 Example of mesh and MPC constraint for the C-ring FEA model.

The simulation results still need improvement in order to capture the experiment results exactly; however, some positives that the asymmetric constitutive model captured is the initiation of phase transformation in tension before compression as well as the max principal strain magnitude. The main difference in the simulation compared to the experimental results is the inherent symmetry in the ABAQUS model compared to reality and testing conditions that produced the experimental data. Although a polar coordinate system would be better to show directional strains, the VIC-2D software used

for DIC could not process with a different coordinate system. Since it used a global Cartesian coordinate system, the preferred strain field to compare the simulation and the experiment is the max principal strain.

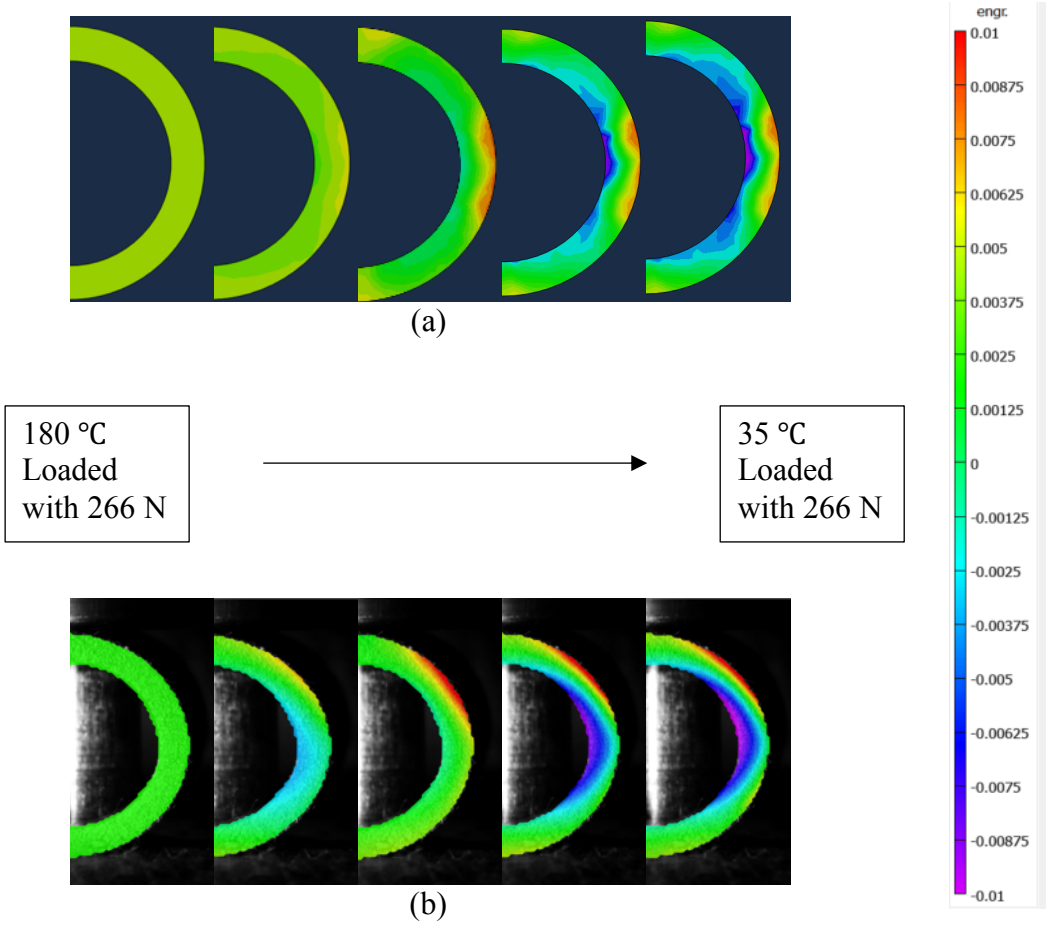

Figure 55 Max principal strain simulation (a) and experiment (b) comparison of forward phase transformation.

4.5 Modeling Improvements

4.5.1 Updated TRIP Evolution

After running through the characterization and modeling implementation, a few limitations to the current UMAT became apparent. While both models work effectively at capturing the cyclic evolution or the tension - compression asymmetry, a single ABAQUS UMAT will be needed to incorporate all of the phenomenon together.

First, the current 1D TRIP strain evolution rate is formulated as an exponential formula:

$$\varepsilon^{l} \; \boldsymbol{h}^{lp} \gamma_1^p C_2^p \left(1 - e^{-\frac{\zeta^d}{C_2^p}}\right) = \varepsilon_{\text{sat}}^p \left(1 - e^{-\frac{\zeta^d}{C_2^p}}\right)$$

As seen by Figure 56, the experimental TRIP strain rate does not saturate for the NITiHf system. A better curve fit would follow a logarithmic strain rate:

$$\boldsymbol{h}^{lp} = C_1 * \ln(1 + C_p * \zeta)$$

$$C_p(\bar{\sigma}) = C_2 * e^{k_p * \bar{\sigma}}$$

This improvement also incorporates a stress dependence as there is typically a larger growth of TRIP depending on the stress applied. ς is the independent variable and is 2N, where N is the number of cycles. C_1, C_2, and k_p are listed in Table 7.

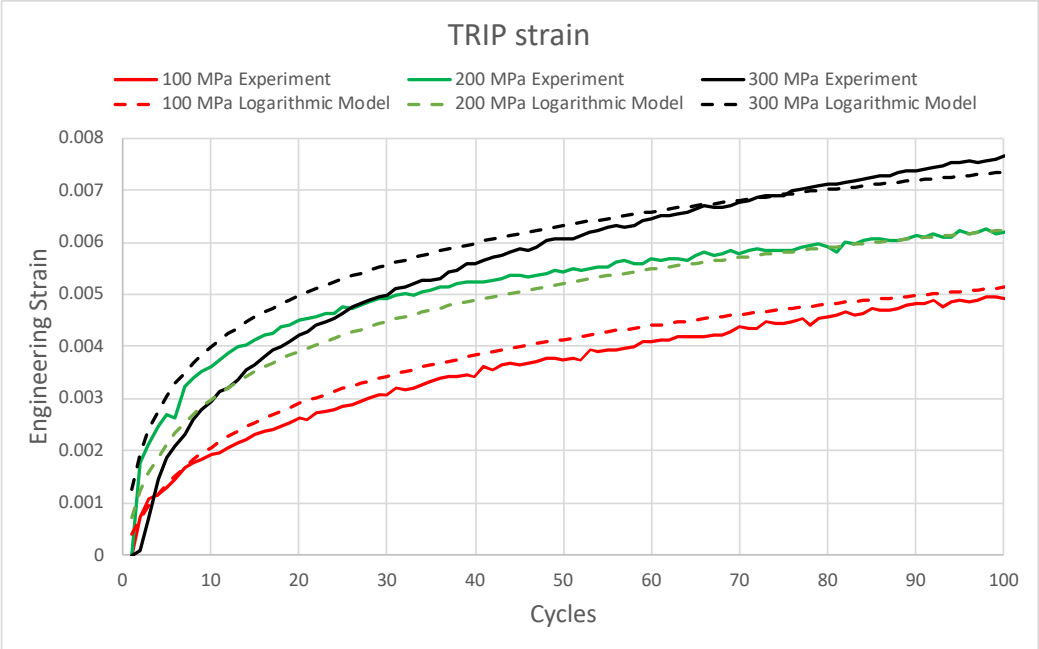

Figure 56 TRIP rate formula modification capturing stress dependence.

Parameter	Value
C_1	0.0015
C_2	0.0700
k_p	0.0075

Table 7 Calculated parameters using the logarithmic and stress dependent TRIP formulation.

5. CONCLUSION

The advancement of structural analysis and simulation efforts is crucial for the design and implementation of morphing actuators. The motivation for this research is to predict the cyclic evolution and the anisotropy of the martensitic phase transformation for High Temperature Shape Memory Alloys (HTSMAs) using commercially available design tools and cost effective testing methods. The experiments for the thermomechanical actuation bending response of polycrystalline HTSMAs, $Ni_{50.3}TiHf_{20}$ (at. %), are designed specifically to allow for development and validation of two phenomenological constitutive models used in recent studies [1, 2]. The finite element software, ABAQUS, with user-defined material subroutines (UMAT), is used to simulate the thermomechanical loading path and the phenomenological response of the SMA phase transformation. Section 4 shows that the models are validated as the finite element simulations match the experimental results relatively accurately. Currently, there are adjustments being made to unify the two models presented, and the experimental data can be useful in calibrating the next versions of the constitutive model.

Since thermomechanical testing of HTSMAs is difficult for standard material testing equipment, custom built test frames are implemented to more effectively capture the macroscopic response. From the test frames, the experimental data shows phenomenon for HTSMAs under cyclic thermomechanical conditions, such as transformation induced plasticity (TRIP), tension - compression asymmetry, and constant actuation strain. During forward phase transformation in an SMA under

bending, tension - compression asymmetry occurs and the zero-strain neutral axis shifts. This is shown experimentally and captured by simulations of four point bending and C-ring compression in ABAQUS. Lastly, the experiments exhibit cyclic evolution after repeated thermomechanical cycling. For SMAs under bending, the combination of tension - compression asymmetry, and the formation of plastic strains during thermomechanical actuation cycling is measured and simulated using both phenomenological constitutive models.

Future work related to this topic will mainly focus on the development and unification of the constitutive models, but additional experiments could be run to highlight interesting features. Three point bending tests could be run on the same test fixture used for four point bending, where experiments could show the influence of the added shear stress state instead of pure bending. Also, experimental results using torque tubes under a cyclic thermomechanical load path would provide more model validation data and component performance of HTSMAs actuators. Lastly, testing specimens with notches, or localized stress concentrations and using the constitutive models to predict the cyclic evolution would be revolutionary for analysis of SMAs.

REFERENCES

[1] Xu, Lei. "A Three-Dimensional Constitutive Modeling for Shape Memory Alloys Considering Two-Way Shape Memory Effect and Transformation-Induced Plasticity." In AIAA Scitech 2019 Forum. San Diego, California: American Institute of Aeronautics and Astronautics, 2019.

[2] Hartl, Darren J., Björn Kiefer, Robin Schulte, and Andreas Menzel. "Computationally-Efficient Modeling of Inelastic Single Crystal Responses via Anisotropic Yield Surfaces: Applications to Shape Memory Alloys." International Journal of Solids and Structures 136–137 (April 1, 2018): 38–59.

[3] Lagoudas, D., ed. Shape Memory Alloys: Modeling and Engineering Applications. New York, NY: Springer, 2008.

[4] D.J. Hartl, D.C. Lagoudas, Aerospace applications of shape memory alloys, Proc Inst Mech Eng, Part G: J Aerospace Eng., 221 (2007), pp. 535-552

[5] Mohd Jani, Jaronie, Martin Leary, Aleksandar Subic, and Mark A. Gibson. "A Review of Shape Memory Alloy Research, Applications and Opportunities." Materials & Design (1980-2015) 56 (April 1, 2014): 1078–1113.

[6] Sofla, A. Y. N., S. A. Meguid, K. T. Tan, and W. K. Yeo. "Shape Morphing of Aircraft Wing: Status and Challenges." Materials & Design 31, no. 3 (March 1, 2010): 1284–92.

[7] Icardi, U., and L. Ferrero. "Preliminary Study of an Adaptive Wing with Shape Memory Alloy Torsion Actuators." Materials & Design 30, no. 10 (December 1, 2009): 4200–4210.

[8] Mabe, J., Cabell, R., and Butler, G. Design and control of a morphing chevron for takeoff and cruise noise reduction. In Proceedings of the 26th Annual AIAA Aeroacoustics Conference, Monterey, CA, 2005, pp. 1–15.

[9] Mabe, J. H., Calkins, F., and Butler, G. Boeing's variable geometry chevron, morphing aerostructure for jet noise reduction. In Proceedings of the 47th AIAA/ASME/ASCE/AHS/ASC Structures, Structural Dynamics and Materials Conference, Newport, Rhode Island, 2006, pp. 1–19.

[10] Hartl, D., Volk, B., Lagoudas, D. C., Calkins, F. T., and Mabe, J. Thermomechanical characterization and modeling of Ni60Ti40 SMA for acutated chevrons. In Proceedings of ASME, International Mechanical Engineering Congress and Exposition (IMECE), Chicago, IL, 5–10 November 2006, pp. 1–10.

[11] Wheeler, Robert, Robert Saunders, Kelli Pickett, Cullen Eckert, Hannah Stroud, Tyler Fink, Kanika Gakhar, James Boyd, and Dimitris Lagoudas. “Design of a Reconfigurable SMA-Based Solar Array Deployment Mechanism,” September 21, 2015, V001T02A010.

[12] Bertagne, C, P Walgren, L Erickson, R Sheth, J Whitcomb, and D Hartl. “Coupled Behavior of Shape Memory Alloy-Based Morphing Spacecraft Radiators: Experimental Assessment and Analysis.” Smart Materials and Structures 27, no. 6 (June 1, 2018): 065006.

[13] RTCA (2010) Do-160g: Environmental conditions and test procedures for airborne equipment. Radio Technical Commission for Aeronautics.

[14] J. Ma, I. Karaman, R.D. Noebe, High temperature shape memory alloys. Int Mater Rev, 55 (2010), pp. 257-315

[15] Kockar B, Karaman I, Kim J I and Chumlyakov Y 2006 A method to enhance cyclic reversibility of NiTiHf high temperature shape memory alloys Scr. Mater. 54 2203–8

[16] Wheeler, Robert, Cade Ottmers, Brett Hewling, and Dimitris Lagoudas. “Actuator Lifetime Predictions for Ni60Ti40 Shape Memory Alloy Plate Actuators.” In Behavior and Mechanics of Multifunctional Materials and Composites 2016, 9800:98000E. International Society for Optics and Photonics, 2016.

[17] T. Tadaki, K. Otsuka, K. Shimizu, Shape memory alloys, Annu Rev Mater Sci, 18 (1988), pp. 25-45

[18] X. Ren, K. Otsuka, Origin of rubber-like behaviour in metal alloys, Nature, 389 (1997), pp. 579-582

[19] Oliveira, Sergio de A., Vanderson M. Dornelas, Marcelo A. Savi, Pedro Manuel C. L. Pacheco, and Alberto Paiva. “A Phenomenological Description of Shape Memory Alloy Transformation Induced Plasticity.” Meccanica 53, no. 10 (August 1, 2018): 2503–23.

[20] W. Huang, W. Toh, Training two-way shape memory alloy by reheat treatment, Mater Sci Lett, 19 (2000), pp. 1549-1550

[21] Perkins J, Hodgson D. The two-way shape memory effect. Butterworth-Heinemann, Engineering Aspects of Shape, Memory Alloys(UK), 1990; 1990. p. 195–206.

[22] Hayrettin, C., O. Karakoc, I. Karaman, J.H. Mabe, R. Santamarta, and J. Pons. “Two Way Shape Memory Effect in NiTiHf High Temperature Shape Memory Alloy Tubes.” Acta Materialia 163 (January 2019): 1–13.

[23] Gall, K., Sehitoglu, H., Chumlyakov, Y., Kireeva, I., 1999b. Tension–compression asymmetry of the stress–strain response in aged single crystal and polycrystalline NiTi. Acta Materialia 47 (4), 1203–1217.

[24] Gall, Ken, and Huseyin Sehitoglu. "The Role of Texture in Tension–Compression Asymmetry in Polycrystalline NiTi." International Journal of Plasticity 15, no. 1 (March 1, 1999): 69–92.

[25] Gall, Ken, Huseyin Sehitoglu, Rob Anderson, Ibrahim Karaman, Yuriy I. Chumlyakov, and Irina V. Kireeva. "On the Mechanical Behavior of Single Crystal NiTi Shape Memory Alloys and Related Polycrystalline Phenomenon." Materials Science and Engineering: A 317, no. 1 (October 31, 2001): 85–92.

[26] Elibol, C., and M.F.-X. Wagner. "Investigation of the Stress-Induced Martensitic Transformation in Pseudoelastic NiTi under Uniaxial Tension, Compression and Compression–Shear." Materials Science and Engineering: A 621 (January 2015): 76–81.

[27] Rallabhandi, Sriram Kishore. "Sonic Boom Minimization through Vehicle Shape Optimization and Probabilistic Acoustic Propagation," April 18, 2005.

[28] Seebass, R. and George, A., "Sonic boom minimization," Journal of Acoustical Society of America, vol. 51, no. 2, pp. 686–694, 1972.

[29] Darden, C., "Sonic boom minimization with nose-bluntness relaxation," Tech. Rep. NASA TP-1348, NASA Langley Research Center, Hampton, VA, Sept. 1979.

[30] Stevens, S., "Perceived level of noise by mark vii and decibels(e)," Journal of the acoustical society of America, vol. 51, no. 2, pp. 575–601, 1972.

[31] Hartl, D J, J H Mabe, O Benafan, A Coda, B Conduit, R Padan, and B Van Doren. "Standardization of Shape Memory Alloy Test Methods toward Certification of Aerospace Applications." Smart Materials and Structures 24, no. 8 (August 1, 2015): 082001.

[32] ASTM 2010 ASTM F2004-05 (2010), *Standard Test Method for Transformation Temperature of Nickel–Titanium Alloys by Thermal Analysis* (West Conshohocken, PA: ASTM International)

[33] ASTM 2006 ASTM F2082-06, *Standard Test Method for Determination of Transformation Temperature of Nickel– Titanium Shape Memory Alloys by Bend and Free Recovery* (withdrawn 2015) (West Conshohocken, PA: ASTM International)

[34] ASTM 2014 ASTM F2516-14, *Standard Test Method for Tension Testing of Nickel–Titanium Superelastic Materials* (West Conshohocken, PA: ASTM International)

[35] ASTM 2015 ASTM E8/E8M-15a, *Standard Test Method for Tension Testing of Metallic Materials* (West Conshohocken, PA: ASTM International)

[36] Calhoun, C., R. Wheeler, T. Baxevanis, and D.C. Lagoudas. "Actuation Fatigue Life Prediction of Shape Memory Alloys under the Constant-Stress Loading Condition." Scripta Materialia 95 (January 2015): 58–61.

[37] Phillips, Francis R., Robert W. Wheeler, Andrew B. Geltmacher, and Dimitris C. Lagoudas. "Evolution of Internal Damage during Actuation Fatigue in Shape Memory Alloys." International Journal of Fatigue 124 (July 2019): 315–27.

[38] Karakoc, O., C. Hayrettin, M. Bass, S.J. Wang, D. Canadinc, J.H. Mabe, D.C. Lagoudas, and I. Karaman. "Effects of Upper Cycle Temperature on the Actuation Fatigue Response of NiTiHf High Temperature Shape Memory Alloys." Acta Materialia 138 (October 2017): 185–97.

[39] Atli, K. C., I. Karaman, R. D. Noebe, G. Bigelow, and D. Gaydosh. "Work Production Using the Two-Way Shape Memory Effect in NiTi and a Ni-Rich NiTiHf High-Temperature Shape Memory Alloy." Smart Materials and Structures 24, no. 12 (November 2015): 125023.

[40] Krar, Steve. "Electrical Discharge Machining," n.d., 3.

[41] Karaca, H. E., S. M. Saghaian, G. Ded, H. Tobe, B. Basaran, H. J. Maier, R. D. Noebe, and Y. I. Chumlyakov. "Effects of Nanoprecipitation on the Shape Memory and Material Properties of an Ni-Rich NiTiHf High Temperature Shape Memory Alloy." Acta Materialia 61, no. 19 (November 1, 2013): 7422–31.

[42] Saghaian, S. M., H. E. Karaca, M. Souri, A. S. Turabi, and R. D. Noebe. "Tensile Shape Memory Behavior of Ni50.3Ti29.7Hf20 High Temperature Shape Memory Alloys." Materials & Design 101 (July 5, 2016): 340–45.

[43] A. Evirgen, I. Karaman, R. Santamarta, J. Pons, R. Noebe, "Microstructural characterization and shape memory characteristics of the Ni50.3Ti34.7Hf15 shape memory alloy," Acta Mater. 83 (2015) 48e60.

[44] O. Karakoc, C. Hayrettin, D. Canadinc, I. Karaman, "Role of applied stress level on the actuation fatigue behavior of NiTiHf high temperature shape memory alloys," Acta Mater. 153 (2018) 156e168.

[45] Roeser, W F, and H T Wensel. "Methods of Testing Thermocouples and Thermocouple. Materials," n.d., 36.

[46] Atli, K. C., I. Karaman, R. D. Noebe, G. Bigelow, and D. Gaydosh. “Work Production Using the Two-Way Shape Memory Effect in NiTi and a Ni-Rich NiTiHf High-Temperature Shape Memory Alloy.” Smart Materials and Structures 24, no. 12 (November 2015): 125023.

[47] Qidwai, M. A., and D. C. Lagoudas. “On Thermomechanics and Transformation Surfaces of Polycrystalline NiTi Shape Memory Alloy Material.” International Journal of Plasticity 16, no. 10 (January 1, 2000): 1309–43.

[48] J. G. Boyd, D. C. Lagoudas. “A thermodynamical constitutive model for shape memory materials.” Part I. The monolithic shape memory alloy, International Journal of Plasticity 12 (6) (1996) 805–842.

[49] Lagoudas, D. C. and Entchev, P. B. “Modeling of transformation-induced plasticity and its effect on the behavior of porous shape memory alloys. Part I: constitutive model for fully dense SMAs,” Mechanics of Materials, Vol. 36, No. 9, 2004, pp. 865–892.

[50] Mirzaeifar, Reza, Reginald DesRoches, Arash Yavari, and Ken Gall. “On Superelastic Bending of Shape Memory Alloy Beams.” International Journal of Solids and Structures 50, no. 10 (May 15, 2013): 1664–80.

[51] FAA 2008 Metallic Materials Properties Development and Standardization (MMPDS) (Washington, DC: Federal Aviation Administration)

[52] Hartl D J and Lagoudas D C. (2008) “Thermomechanical characterization of shape memory alloy materials Shape Memory Alloys: Modeling and Engineering Applications” ed D C Lagoudas (New York: Springer) chapter 2, pp 53–119

[53] Hartl, Darren J., George Chatzigeorgiou, and Dimitris C. Lagoudas. “Three-Dimensional Modeling and Numerical Analysis of Rate-Dependent Irrecoverable Deformation in Shape Memory Alloys.” International Journal of Plasticity 26, no. 10 (October 2010): 1485–1507.

[54] Cazacu, Oana, and Frédéric Barlat. “Generalization of Drucker’s Yield Criterion to Orthotropy.” Mathematics and Mechanics of Solids 6, no. 6 (December 1, 2001): 613–30.